Nonlinear analytical study of structural laminated glass under hard body impact in the pre-crack stage

Xu-Hao Huang[a], Xing-er Wang[b,c,d*], Jian Yang[b,c,e], Zhufeng Pan[b,c], Feiliang Wang[b,c], Iftikhar Azim[b,c]

[a] Key Laboratory of Impact and Safety Engineering, Ministry of Education, Faculty of Mechanical Engineering and Mechanics, Ningbo University, Ningbo, 315211, PR China

[b] State Key Laboratory of Ocean Engineering, Shanghai Jiao Tong University, Shanghai 200240, PR China

[c] Shanghai Key Laboratory for Digital Maintenance of Buildings and Infrastructure, School of Naval Architecture, Ocean and Civil Engineering, Shanghai Jiao Tong University, Shanghai 200240, PR China

[d] Department of Engineering, Lancaster University, Lancaster LA1 4YW, UK

[e] School of Civil Engineering, University of Birmingham, Birmingham B15 2TT, UK

1   **Abstract:** Emerging glass structures, which frequently use laminated glass (LG) as load bearing

2   elements, see a significant rise in recent decade. Existing analytical solutions for LG under impact

3   present limitation when introduced into structural LG products, as structural LG having more glass

4   plies and soft polymeric interlayers requires more accurate nonlinear analytical model. In this study,

5   a nonlinear analytical model was proposed for the simply supported square structural LG subjected

6   to hard body impact. The motion equations were established based on a third order shear

7   deformation theory and von Kármán nonlinear strain-displacement relationship. Based on a two-

8   step perturbation method, the solutions of the motion equations were obtained. The fourth-order

9   Runge-Kutta method was used to capture the impact force variation. Drop weight impact tests with

10   increasing impact velocity, were conducted to record the impact force of LG panels before breakage.

11   Eighteen LG panels with PVB or SG interlayers were tested. Through analysing the fracture

12   initiation from high speed photos as well as the impact force variation in the impact attempt causing

13   fracture, certain feature of the experimental impact force response was determined to be validated

14   with analytical prediction. The validation results show that the proposed model can well reproduce

15   the examined feature and achieve satisfactory impact force response. Case study was then designed

16   to investigate the influence due to the safety windows film on reducing the pre-crack impact

17   response. The effective thickness of LG based on the equivalence of indentation was also proposed

18   for the hard body impact.

19   **Keywords:** Laminated glass; Nonlinear dynamics; Architectural glass; A two-step perturbation

20   method; Hard body impact;

1. Introduction

Structural use of glass, in particular, those glass components acting as load bearing elements commonly require greater redundancy to survive the glass fracture [1, 2]. Therefore, structural laminated glass (LG) products, which comprise more than two glass plies and one polymeric interlayers to achieve better post-fracture performance, have been increasingly used in glass buildings [3]. The most commonly used polymeric interlayers in glass buildings are Polyvinyl Butyral (PVB) [4] and ionoplast interlayers [5]. The impact resistance is one essential factor in the design of glass structures, as glass materials (even thermally toughened glass) present high vulnerability under impacts [6, 7]. Impacts on the structural glass commonly have two types: soft body impact such as manual hit or falling [8-10], or hard body impact like axe attack or windborne debris hit [11, 12]. The structural calculations or experimental study on the soft body impact on the glass products have reached a high level of accuracy [13, 14], which can be found in the existing design code and specifications [15]. However, the hard body impact which yield greater threat to the glass products has less attention.

Most works of the hard body impact on the glass products are carried out by laboratory tests or numerical simulation, which demands the speciality of engineers and facilities [16]. In the laboratory tests, the hard body impactor might be small missiles to simulate windborne debris [17-19], large weight impactor with steel hemispherical head to simulate objects falling [20]. In the automotive engineering, a headform impactor comprising aluminium sphere and Polyvinyl chloride (PVC) skin is designed to simulate human head [21-23]. Wang et al. conducted a series of experiment on testing both pre- and post-fracture behaviour of laminated glass (LG) panels using ionoplast interlayer [20]. The results show the growth trend of the energy dissipation feature and the transverse stiffness under impacts with increasing impact velocities. However, the laboratory tests are expensive and cannot cover as many design variables as the numerical models can. Finite element method (FEM) can be frequently seen in modelling the impact failure of LG products. Most works using FEM focus on developing applicable failure criterion for glass materials [24] or glass-interlayer interface [25, 26]. Other numerical models such as combined finite-discrete element method have also been used in the related topic [27]. Complex mechanical models were developed and implemented into the numerical model [16] to improve the computation accuracy, however, this

2

also brings more difficulties for the engineers to conduct a concise simulation. To have a quick assessment of the impact resistance of glass products, an analytical model might be more practical for designers.

Analytical studies on the impact response of composite laminates can be frequently found. Due to low transverse shear moduli relative to the in-plane Young's moduli, transverse shear deformation plays a much important role in the kinematics of composite laminates. Choi et al. [28] proposed a modified displacement field of plate theory for carbon/epoxy laminates to consider the effect of in-plane pre-load. The analytical contact force history in the low-velocity impact was compared with that from a pendulum impact test. The results show that as the impact energy increases, the analytical result will present higher difference from the experimental result, indicating the impact velocity or impact energy variation needs to be considered in analytical solution. Singh et al. [29] improved a spring-mass system to represent the contact, shear, bending and membrane stiffness of composite laminates. The comparison between FEM result and analytical result shows that the local indentation at impact point should also be considered in a low velocity large mass impact. In Singh's model, the modified contact stiffness was proposed to consider the damage caused by external impact. Wang et al. [30] reviewed eighteen theoretical contact models reported in existing works. It can be found that local indentation is frequently used to characterize the contact behaviour between the impact body and the plate. Therefore, adopting a suitable contact model is a key step in the low-velocity impact model of the laminated structures. Analytical impact model of other composites such as functionally graded carbon nanotube-reinforced composite (FG-CNTRC) [31], carbon fibre reinforced plastics (CFRP) [32], and laminate consisting of polymethyl methacrylate (PMMA) and thermoplastic polyurethane (TPU) [33] under dynamic load can also be found. In contrast, the report on the analytical solution for the LG under low-velocity hard body impact is limited so far. A recent work of Yuan et al. [22] aimed to develop an analytical model for thin automotive LG subjected to low velocity impact of headform impactor. The first-order shear deformation plate theory incorporating the effect of bending, membrane and transverse shear was employed in this model. The peak transverse displacement and contact force from analytical model were compared with that from experimental test. The difference in the contact duration between analytical and testing result was found to be evident, whereas the trend of transverse displacement was satisfactory. Amabili et al. [34] proposed a theoretical model to study the nonlinear dynamic response of laminated glass

plates subjected to blast load. In this model, the geometrically nonlinear damping model [35] was adopted to capture the variation of damping values associated with large-amplitude oscillations of the plate. Other analytical models commonly focus on the static load [36] or blast load [37].

However, as above mentioned, the structural LG is produced via lamination with multiple glass layers, which might be up to 19 mm (e.g. fully tempered glass) for each glass layer. The first order shear deformation theory, which is widely used in the existing analytical works, is very likely to be not applicable in such product, as the multiple "stiff glass - soft polymer" interlaminar deformation is complex. Due to great difference in the material characteristics between the glass layers and the polymeric interlayers, the effect of shear deformation is commonly significant. Therefore, high-order shear deformation plate theories should be used to study the dynamic behaviour of laminated glass panel. At the same time, the contact law used in the analytical model for the laminated glass panel containing the soft-core layer should be modified based on the experimental results. In addition, existing research shows that the increase of impact energy might generate greater deviation of analytical result from realistic one, which has not been well examined. Therefore, in this paper, three novelty points are primarily introduced: 1) the third order shear deformation theory is adopted to consider complex interlaminar deformation, which is more appropriate for structural LG than existing works; 2) the local indentation, which exhibits significant effect on the impact failure due to hard body impact but has not been considered in the existing analytical efforts, is introduced in the proposed model; 3) impact tests are conducted with varying its impact energy, which is then used to examine the potential deviation from the experimental data in the proposed analytical model. Finally, a nonlinear dynamic analytical model can be built for the structural LG under hard body impact with low velocity.

In this work, the impact responses of LG under different impact velocities were investigated theoretically and experimentally. An analytical model considering geometric nonlinearity and shear deformation was presented. The motion equations of the LG and impactor were obtained by combining TSDT with larger deflection theory and framework of Newton's second law of motion, respectively. Furthermore, the second-order differential equation (SODE) including the perturbation solution of the dynamic equation of LG and dynamic equation of impactor can be solved by a fourth order Rung-Kutta method (RK4). The relationship between impact force or indentation and time can be obtained. Drop weight impact tests were subsequently carried out to record the pre-crack

impact force data of LG panels. Followed by a procedure of determining the validated feature of impact force response, the comparison between the analytical and experimental results was finally conducted to examine the applicability of the proposed model. Two case studies: 1) the investigation into the influence of the safety windows film on reducing the pre-crack impact response; 2) the validation of the proposed effective thickness of LG based on the indentation equivalence, were then conducted.

2. Laboratory tests

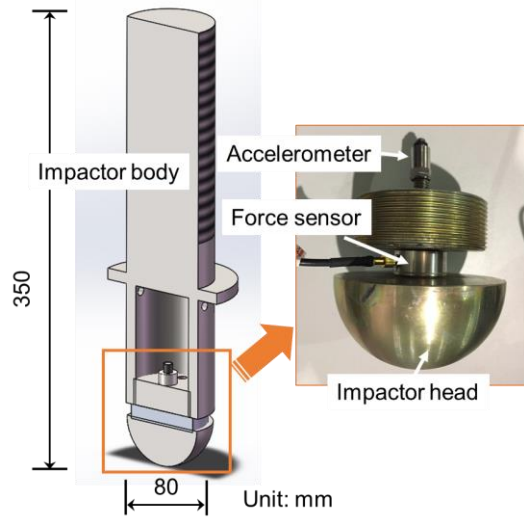## 2.1 Testing apparatus

In this work, the low velocity impact on the structural LG elements is assumed to be caused by large mass impactor such as furniture. A drop weight impact test method with a peak drop height of 6 m was adopted. A transparent guide pipe made of Polymethyl methacrylate (PMMA) was used to drop the impactor (**Fig. 1**(a)). A testing approach characterized by a series of impact attempts with gradually increasing drop heights until glass fracture was adopted. The increment of drop heights was determined as 0.1 m or 0.2 m, which was adjusted according to the expected fracture state of next impact. The impact velocity was then recorded in each impact attempt. It is noting that the repeated impact attempts cannot guarantee precisely identical impact velocity with same drop heights, which is due to the friction of testing system and man-made errors. All sensors were connected to data acquisition units, a sampling frequency of 100 kHz was determined during the tests. Type DH5922N data acquisition unit with multiple sampling modules, which can reach a highest sampling frequency of 256 kHz, was adopted.

Design of the impactor: the large mass impactor made of steel was designed to be a 13.5 kg weight with a spherical head radius of 40 mm and a cylindrical body. A ring-shaped integrated circuit piezoelectric (ICP) force sensor was installed between the head and the impactor body to measure the impact force. The force sensor, type SA-CL600, has a sensitivity of 4 pC/N with response threshold less than 0.01 N. An ICP accelerometer (type SA-PED5W) having a sensitivity of 2 $pC/(m \cdot s^{-2})$ was placed near the impactor head to measure its acceleration (**Fig. 1**(b)).
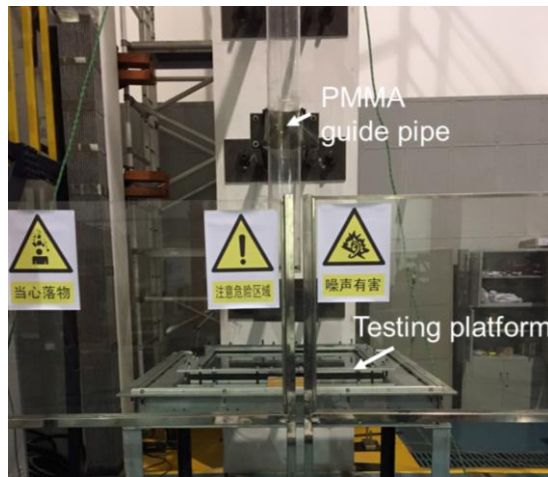
(a) Guide pipe and testing platform   (b) Configuration and details of impactor

1   **Fig. 1** Design of the testing system and impactor

2   Design of the testing platform: the platform was designed to test specimens with a largest size

3   of 1.5 m × 1.5 m (**Fig. 2 (a)**). Considering that the large mass impact will cause too much bouncing

4   and movement of the specimens with simple support, a slight upper constraint was applied at the

5   specimen edge as shown in **Fig. 2 (b).** Although the design was originally for the clamping support,

6   the fixing bolts were adjusted to provide very limited rotational constraint at glass edge in this

7   experiment. A pair of thick neoprene gasket was used to limit the bouncing and movement of the

8   specimen. Through such design, a support condition which was highly close to the simple support

9   can be achieved. The accelerometer glued to the bottom surface of panels beneath impact has a

10   sensitivity of 2 pC/(m·s^{-2}), the nominal threshold is 0.13 g with long-term stability of $\pm$ 1%.

11
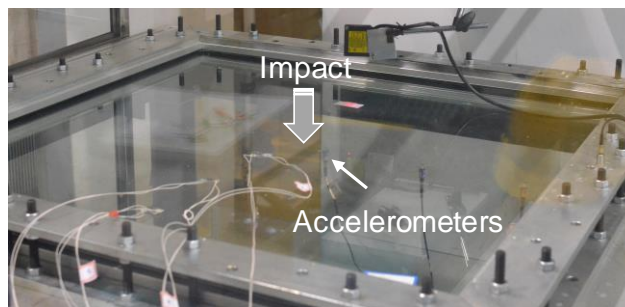
(a) Testing platform and specimen
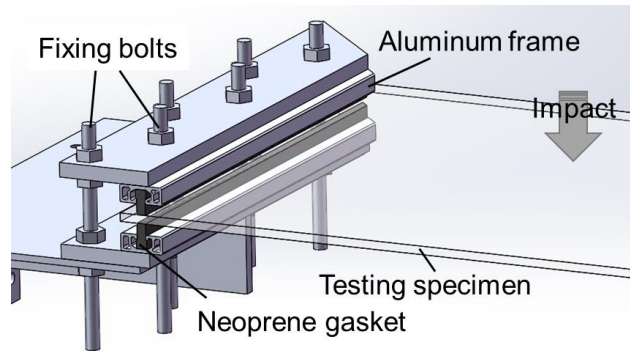
(b) Details of the support condition

1   **Fig. 2** Testing platform and details of the support

2   ## 2.2 Testing specimens

3   18 LG panels split into 2 groups (See **Table 1**) were selected for testing. Fully tempered (FT)

4   glass and two types of interlayers, PVB (Butacite®) and ionoplast (SentryGlas®, SG) interlayers,

5   were utilized to make LG panels. It is noting that, in **Table 1**, because of the discreteness in glass

6   products (e.g., fracture strength of glass, adhesion level between glass and polymer) and impact

7   attempts, the number of impact attempts until fracture were not same. The soda-lime-silica glass

8   products used for the lamination followed the standard requirement of Chinese GB 15763.2 [38].

9   The glass products had edge treatments including polishing before tempering, and its surfaces did

10   not have any treatment. The laminated glass products provided by Henan Zhongbo Glass Co., Ltd

11   followed the standard requirement of Chinese GB 15763.3 [39]. The glass lamination adopted a

12   regular roller prelamination process and autoclaving process. Before lamination, interlayers were

13   packed and transported to the manufacturer without exposure to sunlight.

14   The uniaxial tensile property of PVB material was tested according to GB/T 529 [40] using

15   Instron universal testing machine. The uniaxial tensile tests were performed at ambient temperature

16   of 20 °C with a loading strain rate of 0.2 s^{-1}. The tangent modulus at original point was found to

17   have a mean value of 73.4 MPa, the mean secant modulus at strain of 0.1 was found to be 13 MPa.

18   The ionoplast interlayer was tested under uniaxial tension at the identical ambient temperature and

19   loading strain rate as well. The tangent modulus at original point was around 535 MPa.

20   Several LG panels were tested within each group. Each panel had multiple impact attempts

21   before its fracture. The specimens were sized of 1.0 m × 1.0 m. The nominal thickness of the glass

22   layer and interlayer were 8 mm and 1.52 mm (PVB) or 3.04 mm (SG), respectively. The overlap

1 length of the specimen edges from the support was 15 mm. After testing a total number of 12 PVB

2 LG panels and 6 SG LG panels, the pre-crack impact attempts successfully collected 103 groups of

3 experimental data for PVB LG and 31 groups of data for SG LG.

4

**Table 1** Configuration of the testing specimens

ID	Thermal treatment	Interlayer material	Thickness (mm)	Number of impact attempts	Impact velocity (m·s^{-1})
1-01	Fully tempered	PVB	8/1.52/8	13	0.86 – 1.37
1-02	Fully tempered	PVB	8/1.52/8	1	0.86
1-03	Fully tempered	PVB	8/1.52/8	5	0.92 – 1.27
1-04	Fully tempered	PVB	8/1.52/8	5	0.86 – 1.21
1-05	Fully tempered	PVB	8/1.52/8	4	0.88 – 1.14
1-06	Fully tempered	PVB	8/1.52/8	2	0.86 – 0.97
1-07	Fully tempered	PVB	8/1.52/8	12	1.0 – 1.53
1-08	Fully tempered	PVB	8/1.52/8	22	0.82 – 1.76
1-09	Fully tempered	PVB	8/1.52/8	8	0.82 – 1.29
1-10	Fully tempered	PVB	8/1.52/8	21	0.89 – 1.96
1-11	Fully tempered	PVB	8/1.52/8	12	0.82 – 1.49
1-12	Fully tempered	PVB	8/1.52/8	11	1.01 – 1.43
			Total	103	0.82 – 1.96
2-01	Fully tempered	SG	8/3.04/8	11	0.86 – 1.41
2-02	Fully tempered	SG	8/3.04/8	8	0.91 – 1.27
2-03	Fully tempered	SG	8/3.04/8	2	0.81 – 0.82
2-04	Fully tempered	SG	8/3.04/8	2	0.84 – 0.87
2-05	Fully tempered	SG	8/3.04/8	8	0.64 – 0.95
2-06	Fully tempered	SG	8/3.04/8	1 (N/A)	0.64 (crack)
			Total	31	0.64 -1.41

5

6 ## 2.3 Experimental observation

7 Impact force in the pre-crack impact attempt: the recorded data of ID1-03 (FT/PVB/FT) is

8 taken as example to show the typical time history of impact force (**Fig. 3**) after the impactor contacts

9 the glass panel. It can be seen that there are two contacts within 8 ms. The duration of each contact

10 is around 2.29 ms and 2.83 ms, respectively. As the second contact will not be the predominant hit

11 for cracking the glass, it will not be considered in this study. In the first contact, the oscillation of

12 the force curve is caused by the dynamic coupling effect between impactor and glass panel. Such

13 coupling effect can be frequently seen in the hard body impact, which is due to the interaction

14 between the local high-frequency deformation behaviour of glass material and the impactor

1   movement. The peak impact force can commonly be found at the first or second peak.
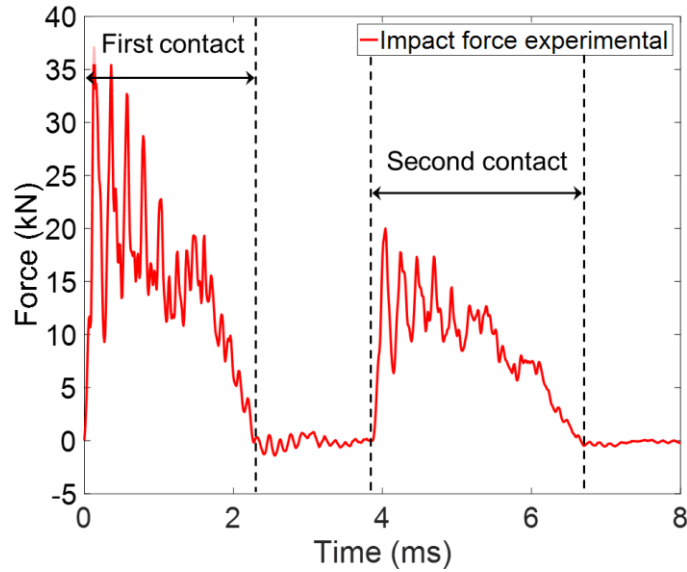
2   **Fig. 3** Typical impact force variation in pre-crack impact attempt

3   Differing from the previous study using soft impactor head, in which the impact force is

4   without oscillation because the interaction force between soft head and glass is not evident, great

5   difficulty rises in seeking the theoretical result of hard body impact when introducing the high-

6   frequency oscillation of impact force. Thus, a rational assumption should be made to simplify the

7   analysis procedure whilst the essential factors are considered. Although the impact force at the first

8   contact has a duration of nearly 2.29 ms in **Fig. 3**, it presents the highest value at the first peak (or

9   second peak in several other impact attempts). It implies that the impact force or the impact energy

10   transferred into the glass panel at the earliest force peaks might dominant the fracture of glass layers.

11   In **Fig. 4**, the normalized impact force curves at fracture in ID1-03, 1-04 and 1-05 are given as

12   example to identify the force peaks which is most likely to determine the glass fracture. It is found

13   that the impact force is more likely declining to zero at nearly 0.4 ms, which indicates the fracture

14   of glass. Such duration commonly includes two force peaks.
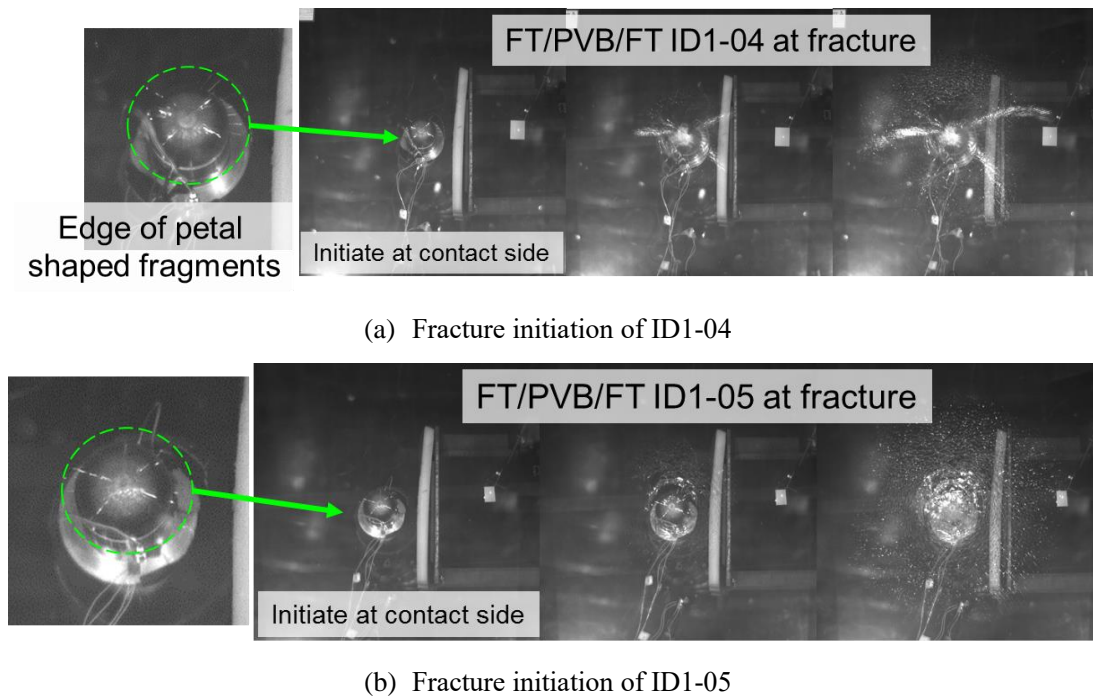
15   The high speed photos at the fracture initiation of ID1-04 and 1-05 are given in **Fig. 5** to better

16   support the determination of the predominant force peaks and its duration. The fractures in ID1-04

17   and 1-05 both initiate at the contact side with the generation of petal shaped fragments near the

18   impact point. After cracks propagating beyond the edge of petal shaped fragments, the FT glass

19   fractures into small dices which are similar to that from the spontaneous breakage (**Fig. 6** (a)). The

20   fracture initiation in the selected specimens is captured at nearly 0.32 – 0.40 ms, which is highly

close to the time at force drop from the impact force curves.
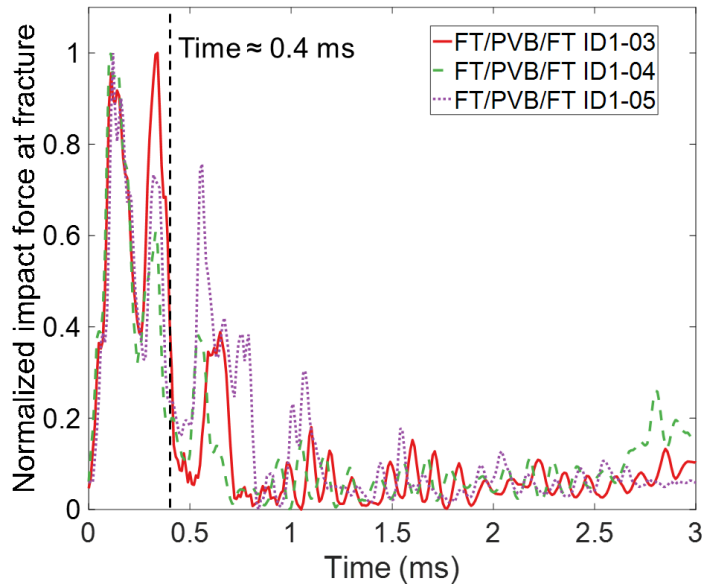
**Fig. 4** Impact force variation in impact attempt causing crack

(a) Fracture initiation of ID1-04

(b) Fracture initiation of ID1-05

Fig. 5 High speed photos of ID1-04 and 1-05 at fracture initiation

Through analysing the fracture pattern, in particular, the petal shaped fragments as well as the fracture initiation and propagation shown in the high speed photos, it can be concluded that the impact failure of glass at contact side is primarily caused by the indentation of the hard impactor head into the glass. As the fracture initiation at the contact side under hard body impact is due to a similar failure process to that in the indentation failure of thermally tempered glass. The crack

10

1　propagation at the impact point is shown in **Fig. 6** (b). A Hertzian cone crack will firstly be formed

2　near the impactor head [41], which is followed by the lateral crack propagation to generate the petal

3　shaped fragments. Whilst, the central crack will propagate vertically beneath the impact point. This

4　is different from the report in the soft body impact, which finds that the fracture commonly initiates

5　at the opposite side with a pattern of radial cracks, indicating that the failure is due to the tensile

6　stress wave. Therefore, it is rational to introduce the indentation movement in the theoretical model

7　of hard body impact to consider such failure mode.

(a)　Fragments at outer glass layer　　　　　(b)　Generating petal shaped fragments
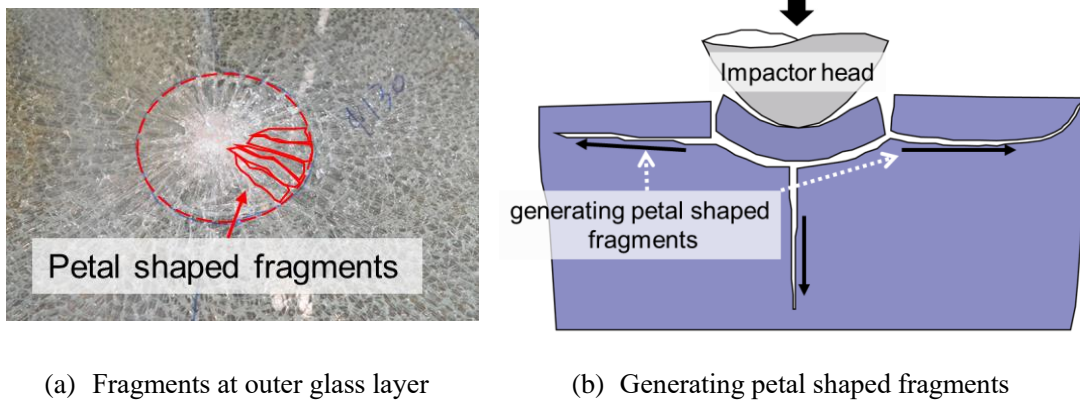
8　**Fig. 6** Fracture pattern from indentation dominant failure

9

10　## 3. Nonlinear dynamic theoretical model

11　In this section, a nonlinear dynamic model is presented for investigating the low velocity

12　impact of LG panels. To simplify the model, the classical Hertz contact law (HCL) is used to

13　characterize the impact response of such structures. It is worth noting that the initial velocity of the

14　impactor is obtained by combining the HCL and introducing a modified coefficient through

15　experiments.

16　### 3.1 Contact model for hard body impact

17　The general contact laws proposed by Meyer was used extensively to capture the indentation

18　of solids. The contact force F_C at different loading stages can be defined as

19　At the loading phase,

$$F_C(t) = K_C \left[\delta(t) \right]^r \tag{1}$$

with $r = 1.5$ is suitable for contact between two isotropic structures. This is also named Hertz's contact law (HCL), which can frequently found in the related works to the impact on LG [42]. However, Abrate [43] found that the HCL was not available to capture the indentation of a sandwich structure. It is then proposed that the index r can be taken as 0.8 by comparing the experimental results with those obtained from Eq.(1).

At the unloading phase,

$$F_C(t) = Q_{max} \left[\frac{\delta(t) - \delta_0}{\delta_{max} - \delta_0} \right]^r \tag{2}$$

where contact stiffness K_C related to the material properties of impactor and face layer of LG is expressed as

$$K_C = \frac{4}{3} \left(\frac{1 - (\mu_{steel})^2}{E_{steel}} + \frac{(\mu_{glass})^2}{E_{glass}} \right)^{-1} \sqrt{R_i} \tag{3}$$

in which E_{steel}, μ_{steel}, and R_i are the material and geometric properties of impactor, respectively (see Sec.4). Q_{max} and δ_{max} are the maximum contact force and local indentation, respectively. The irrecoverable local indentation δ_0 equals to zero when δ_{max} remains below a critical indentation during loading phase. Here, E_P is the elastic modulus of top layer of LG. Considering the effect of out-of-plane Poisson's ratio, Greszczuk [44] proposed a formula for E_P of composite materials with transverse isotropy along the loading direction.

Based on the contact law, a simple way was obtained for studying the effect of the various parameters on the impact response of structure. The initial kinetic energy of the impactor is $T = m_i V^2/2$. Shivakumar et al. [45] showed that the energy can be absorbed by the overall deformation of the plate and local indentation. Based on this assumption, the energy balance equation for the plate can be expressed as:

$$\frac{m_i V_0^2}{2} = U_{bs} + U_m + U_c \tag{4}$$

where U_{bs} is the energy associated with the bending and shear deformations and U_m is the energy associated with membrane deformation. The energy U_{bs} and U_m for plates are defined in [45, 46].

For the HCL, the overall deformation of plate is ignored and the local contact indentation $\delta(t)$

12

is defined as

$$\delta(t) = \overline{W}_i(t) - \overline{W}(X, Y, t) \tag{5}$$

in which $\overline{W}_i(t)$ and $\overline{W}(X, Y, t)$ represent the displacement of impactor and deflection of the LG panels, respectively. The energy stored by indentation can be obtained as follow:

$$U_c = \int_0^{\delta_m} F d\delta = \int_0^{\delta_m} K_c \delta^r d\delta = \frac{(F_m)^{\frac{r+1}{r}}}{(r+1)(K_c)^{1/r}} \tag{6}$$

Therefore, the maximum contact force F_m is written as

$$F_m = k_c \left(\frac{m_i V_0^2 (1+r)}{2k_c} \right)^{\frac{r}{1+r}} \tag{7}$$

In this work, Hertz's assumption of impact on a half-space was adopted. The initial velocity of impactor V_0 can be given by introducing the modified coefficient α.

$$V_0 = \left(\frac{2k_c (F_m / k_c)^{\frac{1+r}{r}}}{m_i (1+r)} \right)^{\frac{1}{2\alpha}} \tag{8}$$

V_0 varies with the maximum contact force F_m obtained by experiment and the $\alpha = 14/15$ (instead of 1 in HCL).

Hence, the motion equation of impactor is given as follow:

$$m_i \ddot{\overline{W}}(t) + F_C(t) = 0, \quad \overline{W}(0) = 0, \dot{\overline{W}}(0) = V_0 \tag{9}$$

where the $m_i = 13.5$ kg is the mass of the impactor.

3.2 Motion equations

Let us consider the LG panels consisting of two glass face sheets and a polymeric interlayer. **Fig. 7** defines the coordinate system used in the analysis of glass panels. The *XYZ* coordinate system is assumed to have its origin on the middle face of the plate, so that the middle surface lies in the *XY*-plane. The displacements at a point in the *X, Y,* and *Z* directions are $\overline{U}, \overline{V}$, and $\overline{W}$, respectively. The size of the panel is taken as $a \times b$ and the total thickness is h.
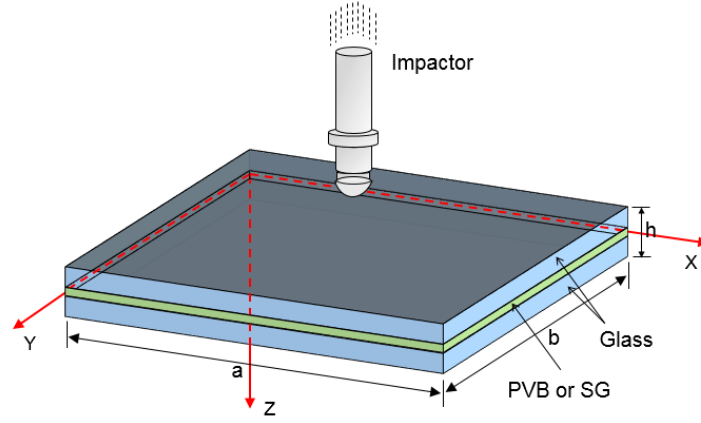
1   **Fig. 7** Glass panels and the reference system adopted

2   The analysing method is based on the third order shear deformation theory [47] for the

3 laminated plate undergoing large deflection. It should be noting that the nonlinear damping effect

4 of PVB or SG interlayer triggered by large deflection is neglected in this model. The investigation

5 of the effect of nonlinear damping on the large amplitude vibration of plate can be found in the

6 recent works of Amalili [35, 48, 49]. In all the cases, a transverse low-velocity impact force Q is

7 considered. The motion equations are given as follow:

$$
\begin{bmatrix}
\tilde{L}_{14}() & -\tilde{L}_{13}() & -\tilde{L}_{12}() & \tilde{L}_{11}() \\
\tilde{L}_{21}() & \tilde{L}_{23}() & \tilde{L}_{22}() & -\tilde{L}_{24}() \\
\tilde{L}_{34}() & -\tilde{L}_{33}() & \tilde{L}_{32}() & \tilde{L}_{31}() \\
\tilde{L}_{44}() & \tilde{L}_{43}() & -\tilde{L}_{42}() & \tilde{L}_{41}()
\end{bmatrix}
\begin{bmatrix}
\bar{F} \\
\bar{\Psi}_y \\
\bar{\Psi}_x \\
\bar{W}
\end{bmatrix}
=
\begin{bmatrix}
1 & \tilde{L}_{17}() & I_8\dfrac{\partial()}{\partial X} & I_8\dfrac{\partial()}{\partial Y} \\
0 & 0 & 0 & 0 \\
0 & I_9\dfrac{\partial()}{\partial X} & I_{10} & 0 \\
0 & I_9\dfrac{\partial()}{\partial Y} & 0 & I_{10}
\end{bmatrix}
\begin{bmatrix}
Q \\
\ddot{\bar{W}} \\
\ddot{\bar{\Psi}}_x \\
\ddot{\bar{\Psi}}_y
\end{bmatrix}
$$

$$
+
\begin{bmatrix}
\tilde{L}(\bar{W},\bar{F}) \\
-\dfrac{1}{2}\tilde{L}(\bar{W},\bar{W}) \\
0 \\
0
\end{bmatrix}
\tag{10}
$$

8   where the nonlinear operator $(\tilde{L}())$ and the stress function $(\bar{F})$ can be expressed as follow:

$$
\tilde{L}(\ ) = \frac{\partial^2}{\partial X^2}\frac{\partial^2}{\partial Y^2} - 2\frac{\partial^2}{\partial X \partial Y}\frac{\partial^2}{\partial X \partial Y} + \frac{\partial^2}{\partial Y^2}\frac{\partial^2}{\partial X^2}
\tag{11}
$$

$$
\bar{N}_x = \partial^2 \bar{F}/\partial Y^2, \quad \bar{N}_{xy} = \partial^2 \bar{F}/\partial X \partial Y, \quad \bar{N}_y = \partial^2 \bar{F}/\partial X^2
\tag{12}
$$

9        $\bar{\Psi}_x$ and $\bar{\Psi}_y$ denote the rotation about the Y- and X–axis, respectively. The coefficients S_{ij} and

1   inertias I_i (i=8, 9, 10) are given in Appendix A. The operators $(\tilde{L}_{ij}())$ introduced in the above motion

2   equations are defined from [50].

3   In the current work, immovable in-plane boundary conditions (BCs) are considered as follows.

4   at $X=0$, a:

$$\overline{W} = \overline{\Psi}_y = \overline{M}_x = \overline{P}_x = 0 \tag{13}$$

$$\overline{U} = 0 \tag{14}$$

5   at $Y=0$, b:

$$\overline{W} = \overline{\Psi}_x = \overline{M}_y = \overline{P}_y = 0 \tag{15}$$

$$\overline{V} = 0 \tag{16}$$

6   in which the quantities $(\overline{M}_x, \overline{M}_y)$ denote the flexural moments and $(\overline{P}_x, \overline{P}_y)$ represent the higher

7   order moments given by [47].

8   The immovable BCs are converted to integral form as given below:

$$\int_0^b \int_0^a \frac{\partial \overline{U}}{\partial X} dX dY = 0 \tag{17}$$

$$\int_0^a \int_0^b \frac{\partial \overline{V}}{\partial Y} dY dX = 0 \tag{18}$$

9   where,

$$\frac{\partial \overline{U}}{\partial X} = A_{11}^* \frac{\partial^2 \overline{F}}{\partial Y^2} + \left(B_{12}^* - \frac{4E_{12}^*}{3h^2} \right) \frac{\partial \overline{\Psi}_y}{\partial Y} + A_{12}^* \frac{\partial^2 \overline{F}}{\partial X^2} + \left(B_{11}^* - \frac{4E_{11}^*}{3h^2} \right) \frac{\partial \overline{\Psi}_x}{\partial X}$$
$$- \frac{4}{3h^2} \left(E_{21}^* \frac{\partial^2 \overline{W}}{\partial X^2} + E_{22}^* \frac{\partial^2 \overline{W}}{\partial Y^2} \right) - \frac{1}{2} \left(\frac{\partial \overline{W}}{\partial X} \right)^2 \tag{19}$$

10

$$\frac{\partial \overline{V}}{\partial Y} = A_{22}^* \frac{\partial^2 \overline{F}}{\partial X^2} + A_{12}^* \frac{\partial^2 \overline{F}}{\partial Y^2} + \left(B_{21}^* - \frac{4E_{21}^*}{3h^2} \right) \frac{\partial \overline{\Psi}_x}{\partial X} + \left(B_{22}^* - \frac{4E_{22}^*}{3h^2} \right) \frac{\partial \overline{\Psi}_y}{\partial Y}$$
$$- \frac{4}{3h^2} \left(E_{21}^* \frac{\partial^2 \overline{W}}{\partial X^2} + E_{22}^* \frac{\partial^2 \overline{W}}{\partial Y^2} \right) - \frac{1}{2} \left(\frac{\partial \overline{W}}{\partial X} \right)^2 \tag{20}$$

11   where the reduced stiffness $(A_{ij}^*, B_{ij}^*, D_{ij}^*, E_{ij}^*, F_{ij}^*, H_{ij}^*)$ are the functions of the geometry,

12   materials properties, and stacking sequence of the LG panels as given in Appendix A.

13   Here, a two-step perturbation approach technology [50] is used to solve the nonlinear equations.

14   Eq. (10) can be converted to dimensionless forms by the definition of the following dimensionless

1   parameters as:

$$
2 \quad
\begin{bmatrix}
\gamma_{14}L_{14}() & -L_{13}() & -L_{12}() & L_{11}() \\
L_{21}() & \gamma_{24}L_{23}() & \gamma_{24}L_{22}() & -\gamma_{24}L_{24}() \\
\gamma_{14}L_{34}() & -L_{33}() & L_{32}() & L_{31}() \\
\gamma_{14}L_{44}() & L_{43}() & -L_{42}() & L_{41}()
\end{bmatrix}
\begin{bmatrix}
F \\ \Psi_y \\ \Psi_x \\ W
\end{bmatrix}
=
\begin{bmatrix}
1 & L_{17}(\ddot{W}) & \gamma_{80}\dfrac{\partial()}{\partial x} & \gamma_{80}\beta\dfrac{\partial()}{\partial y} \\
0 & 0 & 0 & 0 \\
0 & \gamma_{90}\dfrac{\partial()}{\partial x} & \gamma_{10} & 0 \\
0 & \gamma_{90}\beta\dfrac{\partial()}{\partial y} & 0 & \gamma_{10}
\end{bmatrix}
\begin{bmatrix}
\lambda_q \\ \ddot{W} \\ \ddot{\Psi}_x \\ \ddot{\Psi}_y
\end{bmatrix}
$$

$$
+
\begin{bmatrix}
\gamma_{14}\beta^2 L(W,F) \\
-\dfrac{1}{2}\gamma_{24}\beta^2 L(W,W) \\
0 \\
0
\end{bmatrix}
\tag{21}
$$

3   It is convenient to introduce dimensionless parameters and nonlinear operator ($L()$).

4

$$
(W,F)=\left(\frac{\bar{W}}{[D_{11}^{*}D_{22}^{*}A_{11}^{*}A_{22}^{*}]^{1/4}},\frac{\bar{F}}{[D_{11}^{*}D_{22}^{*}]^{1/2}}\right),\ (x,y,\beta)=\left(\pi\frac{X}{a},\pi\frac{Y}{b},\frac{a}{b}\right)
$$

$$
(\gamma_5,\gamma_{14},\gamma_{24})=\left(-\frac{A_{12}^{*}}{A_{22}^{*}},\sqrt{\frac{D_{22}^{*}}{D_{11}^{*}}},\sqrt{\frac{A_{11}^{*}}{A_{22}^{*}}}\right),\ \gamma_{170}=-\frac{I_1 E_0 a^2}{D_{11}^{*}\pi^2\rho_0},\ \gamma_{171}=\frac{4(I_5 I_1 - I_4 I_2)E_0}{3D_{11}^{*}h^2 I_1\rho_0}
$$

$$
\begin{bmatrix}
\Psi_x & \Psi_y \\
M_x & P_x
\end{bmatrix}
=\frac{a}{\pi[A_{11}^{*}D_{11}^{*}A_{22}^{*}D_{22}^{*}]^{1/4}}
\begin{bmatrix}
\bar{\Psi}_x & \bar{\Psi}_y \\
\dfrac{a\bar{M}_x}{D_{11}^{*}\pi} & \dfrac{4a\bar{P}_x}{3h^2 D_{11}^{*}\pi}
\end{bmatrix},\ t=\frac{\pi\bar{t}}{a}\sqrt{\frac{E_0}{\rho_0}}
$$

$$
(\gamma_{10},\gamma_{80},\gamma_{90})=(I_{10},I_8,I_9)\frac{E_0}{\rho_0 D_{11}^{*}},\ (\lambda_x,\lambda_y)=\frac{h(\sigma_x b^2,\sigma_y a^2)}{4\pi^2\sqrt{D_{11}^{*}D_{22}^{*}}},
$$

$$
\lambda_q=\frac{a^4 Q}{D_{11}^{*}\pi^4[A_{11}^{*}D_{11}^{*}A_{22}^{*}D_{22}^{*}]^{1/4}},\ L(\ )=\frac{\partial^2}{\partial X^2}\frac{\partial^2}{\partial Y^2}+\frac{\partial^2}{\partial Y^2}\frac{\partial^2}{\partial X^2}-2\frac{\partial^2}{\partial X\partial Y}\frac{\partial^2}{\partial X\partial Y}.
$$

$$
\tag{22}
$$

5   in which $E_0=E_{\text{glass}}$, $\rho_0=\rho_{\text{glass}}$. In Eq. (21), the dimensionless linear operators ($L_{ij}()$) are defined

6   in [50]. γ_{170} and γ_{171} are used in Eq.(40.a).

7   Substitution of dimensionless parameters into Eqs. (13), (15) and (19)-(20) yields:

8   at $x=0$, a:

$$
W=\Psi_y=M_x=P_x=0
\tag{23}
$$

16

$$\int_0^\pi \int_0^\pi \left[\gamma_{24}^2 \beta^2 \frac{\partial^2 F}{\partial y^2} - \gamma_5 \frac{\partial^2 F}{\partial x^2} + \gamma_{24} \left(\gamma_{511} \frac{\partial \Psi_x}{\partial x} + \gamma_{223} \beta \frac{\partial \Psi_y}{\partial y} \right) \right.$$

$$\left. - \gamma_{24} \left(\gamma_{244} \beta^2 \frac{\partial^2 W}{\partial y^2} + \gamma_{611} \frac{\partial^2 W}{\partial x^2} \right) - \frac{1}{2} \gamma_{24} \left(\frac{\partial W}{\partial x} \right)^2 \right] dxdy = 0 \tag{24}$$

at $y = 0, b$:

$$W = \Psi_x = M_y = P_y = 0 \tag{25}$$

$$\int_0^\pi \int_0^\pi \left[\frac{\partial^2 F}{\partial x^2} - \gamma_5 \beta^2 \frac{\partial^2 F}{\partial y^2} + \gamma_{24} \left(\gamma_{220} \frac{\partial \Psi_x}{\partial x} + \gamma_{522} \beta \frac{\partial \Psi_y}{\partial y} \right) \right.$$

$$\left. - \gamma_{24} \left(\gamma_{240} \frac{\partial^2 W}{\partial x^2} + \gamma_{622} \beta^2 \frac{\partial^2 W}{\partial y^2} \right) - \frac{\gamma_{24} \beta^2}{2} \left(\frac{\partial W}{\partial y} \right)^2 \right] dxdy = 0 \tag{26}$$

with γ_{ijk} given in Shen [50].

3.3 Solutions for the low velocity impact

The solutions for Eq. (21) consist of an additional displacement and rotation terms as a result of the impact loading. The following initial BCs are adopted in the present work:

$$W(x,y,t)|_{t=0} = \frac{\partial W(x,y,t)}{\partial t}|_{t=0} = 0,$$

$$\Psi_x(x,y,t)|_{t=0} = \frac{\partial \Psi_x(x,y,t)}{\partial t}|_{t=0} = 0, \tag{27}$$

$$\Psi_y(x,y,t)|_{t=0} = \frac{\partial \Psi_y(x,y,t)}{\partial t}|_{t=0} = 0.$$

A two-step perturbation technique is applied to determine the solution. Considering $\tau = \varepsilon t$, the solution equations can be expanded as a function with a small perturbation parameter ε^j ($j=1, 2, 3, \ldots$) which has no physical meaning.

$$W(x,y,\tau,\varepsilon) = \varepsilon w_1(x,y,\tau) + \varepsilon^2 w_2(x,y,\tau) + \varepsilon^3 w_3(x,y,\tau) + \cdots$$

$$\Psi_x(x,y,\tau,\varepsilon) = \varepsilon \psi_{x1}(x,y,\tau) + \varepsilon^2 \psi_{x2}(x,y,\tau) + \varepsilon^3 \psi_{x3}(x,y,\tau) + \cdots$$

$$\Psi_y(x,y,\tau,\varepsilon) = \varepsilon \psi_{y1}(x,y,\tau) + \varepsilon^2 \psi_{y2}(x,y,\tau) + \varepsilon^3 \psi_{y3}(x,y,\tau) + \cdots$$

$$F(x,y,\tau,\varepsilon) = f_0(x,y,\tau) + \varepsilon f_1(x,y,\tau) + \varepsilon^2 f_2(x,y,\tau) + \cdots$$

$$\lambda_q(x, y, \tau, \varepsilon) = \varepsilon \lambda_1(x, y, \tau) + \varepsilon^2 \lambda_2(x, y, \tau) + \varepsilon^3 \lambda_3(x, y, \tau) + \cdots$$

(28)

1   Following the perturbation solutions procedure, one assumes the following form of the first

2   term of $w_j(x, y, \tau)$ that satisfies the simply supported BCs:

$$w_1(x, y, \tau) = A_{11}^{(1)}(\tau) \sin mx \sin ny,$$

(29)

3   where the terms (m, n) are used to describe the waveform. For immovable BCs, $f_0(x, y)=$-

4    $B_{00}^{(0)} y^2/2$-$b_{00}^{(0)} y^2/2$. Motion equations converted into their perturbation expansions are given from the

5   substitution of solution equations (28) to Eq. (21). The asymptotic solutions obtained for the

6   perturbation equations with order equal to $\varepsilon=1, 2, 3$ are given below:

$$W(x, y, t) = \varepsilon[A_{11}^{(1)}(t) \sin mx \sin ny] + \varepsilon^3 [A_{13}^{(3)}(t) \sin mx \sin 3ny$$

$$+ A_{31}^{(3)}(t) \sin 3mx \sin ny] + O(\varepsilon^4)$$

(30)

$$\Psi_x(x, y, t) = \varepsilon[C_{11}^{(1)}(t) + \ddot{C}_{11}^{(3)}(t)] \cos mx \sin ny + \varepsilon^2 C_{20}^{(2)}(t) \sin 2mx$$

$$+ \varepsilon^3 [C_{13}^{(3)}(t) \cos mx \sin 3ny + C_{31}^{(3)}(t) \cos 3mx \sin ny] + O(\varepsilon^4)$$

(31)

$$\Psi_y(x, y, t) = \varepsilon[D_{11}^{(1)}(t) + \ddot{D}_{11}^{(3)}(t)] \sin mx \cos ny + \varepsilon^2 D_{02}^{(2)}(t) \sin 2ny$$

$$+ \varepsilon^3 [D_{13}^{(3)}(t) \sin mx \cos 3ny + D_{31}^{(3)}(t) \sin 3mx \cos ny] + O(\varepsilon^4)$$

(32)

$$F(x, y, t) = -\frac{B_{00}^{(0)} y^2}{2} - \frac{b_{00}^{(0)} x^2}{2} + \varepsilon[B_{11}^{(1)}(t) + \ddot{B}_{11}^{(3)}(t)] \sin mx \sin ny$$

$$+ \varepsilon^2 \left(-\frac{B_{00}^{(2)} y^2}{2} - \frac{b_{00}^{(2)} x^2}{2} + B_{02}^{(2)}(t) \cos 2ny + B_{20}^{(2)}(t) \cos 2mx \right)$$

$$+ \varepsilon^3 [B_{13}^{(3)}(t) \sin mx \sin 3ny + B_{31}^{(3)}(t) \sin 3mx \sin ny] + O(\varepsilon^4)$$

(33)

$$\lambda_q(x, y, t) = \varepsilon[g_1 A_{11}^{(1)}(t) + g_4 \ddot{A}_{11}^{(1)}(t)] \sin mx \sin ny$$

$$+ (\varepsilon A_{11}^{(1)}(t))^2 \left(g_{02} \cos 2ny + g_{20} \cos 2mx \right)$$

$$+ (\varepsilon A_{11}^{(1)}(t))^3 g_3 \sin mx \sin ny + O(\varepsilon^4)$$

(34)

7   It is noting that the perturbation series is a divergent series, in which the order solution is closer

8   to the real solution and needs to be determined by experimental verification or by comparing with

9   the theoretical exact solution. Zhang [51] and Shen [52] found that there were no such things as

18

1 higher order perturbation solution being more correct than lower order solution. According to

2 previous work [53-55], it is found that the 3rd order asymptotic solution can be used to study large-

3 amplitude vibration.

4 In Eq.(30), $\varepsilon A_{11}^{(1)}(t)$ is considered as the second perturbation parameter which is the function

5 of the deflection, By taking $(x, y)=(\pi/2m, \pi/2n)$, $\varepsilon A_{11}^{(1)}(t)$ can be expressed as:

$$\varepsilon A_{11}^{(1)}(t) = W_m - \Theta_1 W_m^3 + \cdots \tag{35}$$

6 Substituting equation (35) into equation (34) and applying Galerkin procedure, one has

$$g_{40} \frac{d^2(W_m)}{dt^2} + g_{41}(W_m) + g_{42}(W_m)^2 + g_{43}(W_m)^3 = \bar{\lambda}_q(t) \tag{36}$$

7 where

$$\bar{\lambda}_q(t) = \frac{4}{\pi^2} \int_0^\pi \int_0^\pi \lambda_q(x, y, t) \sin mx \sin ny \, dx dy \cdot \tag{37}$$

8 When the $\bar{\lambda}_q(t)=0$, the Eq. (36) becomes duffing equation corresponding to the larger

9 amplitude vibration of plate. Here, we take $\bar{\lambda}_q(t)=F_c(t)$ to consider low velocity impact of panel.

10 the SODEs of both the LG panel and the impactor can be rewritten as:

$$g_{40} \frac{d^2(\varepsilon A_{11}^{(1)})}{dt^2} + g_{41}(\varepsilon A_{11}^{(1)}) + g_{42}(\varepsilon A_{11}^{(1)})^2 + g_{43}(\varepsilon A_{11}^{(1)})^3 - g_{44} \left[W_i(t) - W(t) \right]^r = 0 \tag{38}$$

$$\frac{d^2 W_i(t)}{dt^2} = -g_{45} \left[W_i(t) - W(t) \right]^r \tag{39}$$

11 Hence, the SODEs with initial value $(W(0)=\dot{W}(0)=W_i(0)=0, \dot{W}_i(0)=v)$ can be solved by

12 employing the RK4 numerical method that has been used to study low velocity impact behaviour of

13 composited structures [56-58]. $g_{40}, g_{41},\ldots$et al. are given as follows.

$$g_{40} = -[\gamma_{170} - \gamma_{171}(m^2 + n^2\beta^2)] - g_{08}^* - \gamma_{14}\gamma_{24} \frac{g_{05}^* g_{07}}{g_{06}}$$

$$+\gamma_{80} \left(\gamma_{14}\gamma_{24} \frac{m^2 g_{02} + n^2\beta^2 g_{01}}{g_{00}} \frac{g_{05}}{g_{06}} - \frac{m^2 g_{04} + n^2\beta^2 g_{03}}{g_{00}} \right), \tag{40.a}$$

$$g_{41} = g_{08} + g_{05}g_{07} \frac{\gamma_{14}\gamma_{24}}{g_{06}}, \tag{41.b}$$

$$g_{42} = \frac{-2mn\beta^2\gamma_{14}\gamma_{24}}{3\pi^2} \left(4\frac{g_{05}}{g_{06}} + \frac{\gamma_8}{\gamma_6} + \frac{\gamma_9}{\gamma_7} \right)(1-\cos m\pi)(1-\cos n\pi), \tag{42.c}$$

19

$$g_{43} = \frac{\gamma_{14}\gamma_{24}}{16}\left(C_{33} + \frac{(n\beta)^4}{\gamma_6} + \frac{m^4}{\gamma_7}\right), C_{33} = 2\frac{m^4 + \gamma_{24}^2 n^4 \beta^4 + 2\gamma_5 m^2 n^2 \beta^2}{\gamma_{24}^2 - \gamma_5^2} \qquad (43.d)$$

$$g_{44} = \frac{4K_c a^2 \left(A_{11}^* A_{22}^* D_{11}^* D_{22}^*\right)^{1/8}}{\pi^4 D_{11}^*} \sin\frac{m\pi}{2}\sin\frac{n\pi}{2} \qquad (44.e)$$

$$g_{45} = \frac{\rho_0 K_c a^2 \left(A_{11}^* A_{22}^* D_{11}^* D_{22}^*\right)^{1/8}}{E_0 \pi^2 m^i} \qquad (45.d)$$

with the other symbols are given in Shen [50].

4. Validation and discussion

(1) PVB laminated glass panels:

The material properties used in the validation of pre-crack behavior in PVB LG panels are as follows: elastic modulus: E_{glass} = 70 GPa, E_{PVB} = 267 MPa, E_{steel} = 200 GPa; density: ρ_{glass} = 2500 kg·m^{-3}, ρ_{PVB} = 1000 kg·m^{-3}, ρ_{steel} = 7960 kg·m^{-3}; Poisson's ratio: μ_{glass} = 0.22, μ_{PVB} = 0.45, μ_{steel} = 0.3. It is worth noting that PVB material is highly sensitive to the strain rate, which will shift from rubbery material to glassy elasto-plastic material with stiffness increase when strain rate increases from 10^{-2} s^{-1} level to 10^2 s^{-1} level [59]. In this work, the low velocity impact is expected to generate a strain rate level of 10^2 s^{-1} in interlayer. The elastic modulus of PVB material in this section is determined based on Zhang's work [60], which gives a simplified formula (see equation (41)) for calculating the initial modulus of PVB under high strain rates.

$$E_{ini} = 129.49 \log_{10}(\frac{\dot{\varepsilon}}{\dot{\varepsilon}_0}) - 92.275 \qquad \dot{\varepsilon} > 10s^{-1} \qquad (41)$$
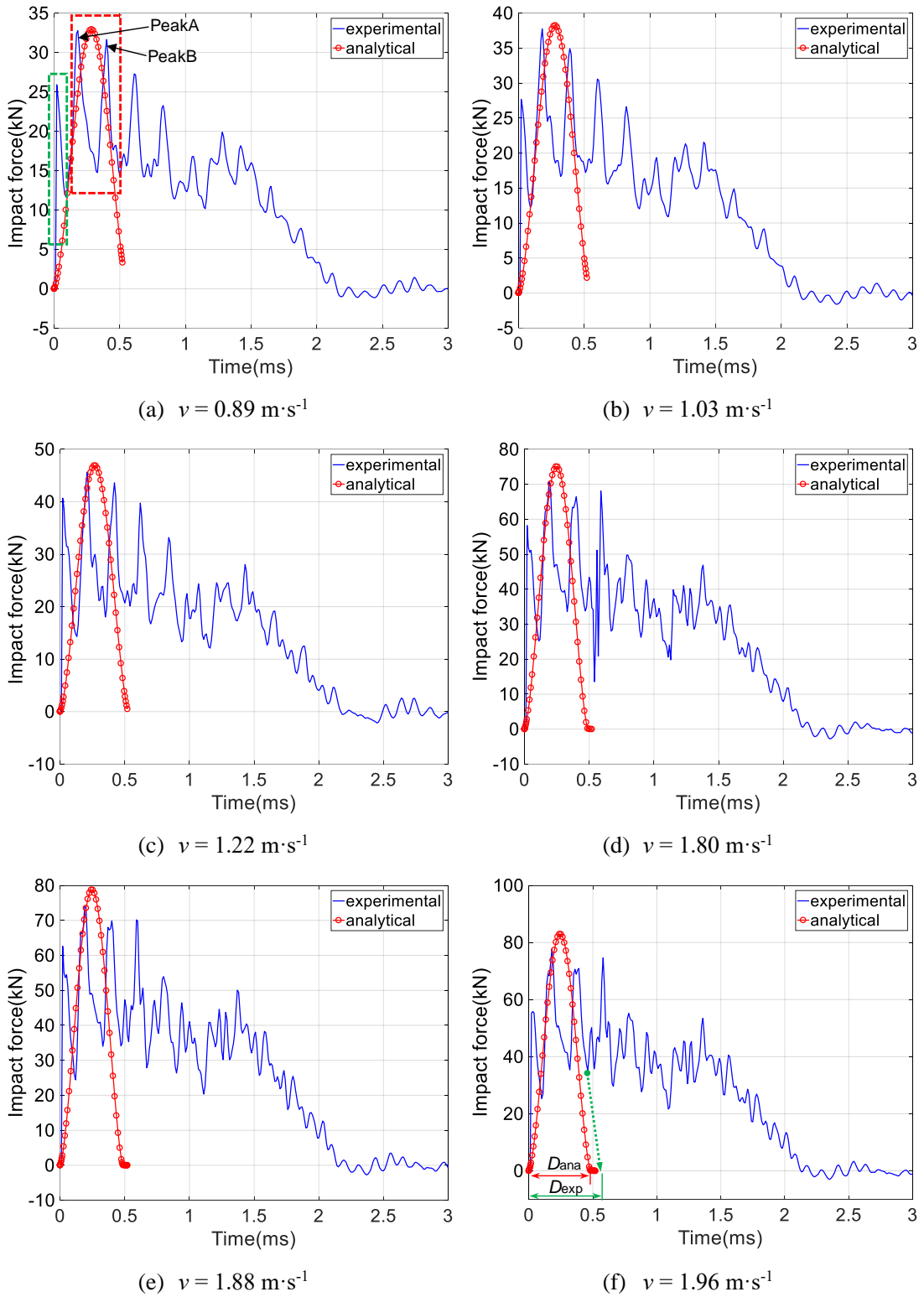
where E_{ini} is the initial modulus, which is taken as the elastic modulus in this section. $\dot{\varepsilon}$ is the strain rate, $\dot{\varepsilon}_0$ is reference strain rate of 1 s^{-1}. Based on the preliminary works of numerical prediction, the strain rate might be more than 200 s^{-1} and can reach 600 s^{-1}. The elastic modulus of PVB is then calculated based on equation (41) and its value is found to vary from 206 MPa to 267 MPa. Here, the elastic modulus E_{PVB} is taken as 267 MPa.

Considering that the recorded impact velocity of specimen ID1-10 can cover the testing velocity range in PVB LG panels, it is taken as an example to validate the experimental data with that from the proposed model. Six cases from velocity, v, of 0.89 m·s^{-1} to 1.96 m·s^{-1} are shown in **Fig. 8** to give a comparison between analytical result and experimental data. It is worth noting that

the first peak in the experimental curve (highlighted by green box in **Fig. 8** (a)) is not the "first peak"

in **Fig. 3**. The highlighted peak is actually referring to the negligible peak at nearly 0.06 ms in **Fig.**

3 (see also in **Fig. 4**), which has a much lower value than the peak force at nearly 0.18 ms. The

analytical model is expected to have a satisfactory prediction for the second and third peaks of

experimental results (highlighted by red box in **Fig. 8** (a)). Thus, the first peak will not be discussed.

From **Fig. 8** (a), it can be seen that the analytical curve grows with a highly close path to that

of the peak (PeakA) which initiates from 0.09 ms and reaches its highest value at 0.18 ms. The

analytical curve drops at nearly 0.28 ms and its decline also follows a similar path to that of PeakB.

The analytical peak can be found at almost the same location of the center (0.29 ms) between PeakA

and PeakB, where a trough of experimental data can be found. Such trough indicates that the glass

material beneath the impactor head experienced a short vibration period during the indentation

movement of impactor from 0.18 ms (PeakA) to 0.4 ms (PeakB) and hence generates a very fast

contact (PeakA), detachment (trough) and the next contact (PeakB). If this short vibration of local

glass material at contact is removed, the peak instead is very likely to be the same as that in analytical

result. In addition, the analytical peak force is 32.9 kN whilst that of experimental result in PeakA

is 32.8 kN, showing a good agreement. Thus, it can be concluded that the analytical prediction has

achieved the expected result in the examined impact velocity of 0.89 m·s^{-1}.

From **Fig. 8** (b) to (f), it can be observed that, with the velocity increase the declining path of

analytical result has a trend of being deviated from the declining path of experimental PeakB. It

shows that the predicted duration (see D_{ana} in **Fig. 8** (f)) is less than the experimental one covered

by PeakA and PeakB (see D_{exp} in **Fig. 8** (f)). It is then found that, with the increasing deviation and

underestimation on the contact duration, the difference of peak force has a rise from the case of $v =$

0.89 m·s^{-1} (0.1 kN) to that of $v = 1.96 \text{ m·s}^{-1}$ (5.3 kN). Although the absolute force difference has an

increase, the relative proportion to the experimental peak force is around 6.8% in case with $v = 1.96$

m·s^{-1}, which still can be accepted. As for the latter part from time $= D_{exp}$ to that where force drops

to zero, the keep-in contact between glass and impactor is more likely caused by the deformation of

the entire laminated glass panel and the movement of impactor, whereas the maximum indentation

into the glass material does not have a significant increase. Thus, as the indentation and its associated

pre-crack behaviour (highlighted by red box in **Fig. 8** (a)) are the examined feature in this work, the

latter part will not be included in discussion and analytical effort.

(a) $v = 0.89$ m·s^{-1}

(b) $v = 1.03$ m·s^{-1}

(c) $v = 1.22$ m·s^{-1}

(d) $v = 1.80$ m·s^{-1}

(e) $v = 1.88$ m·s^{-1}
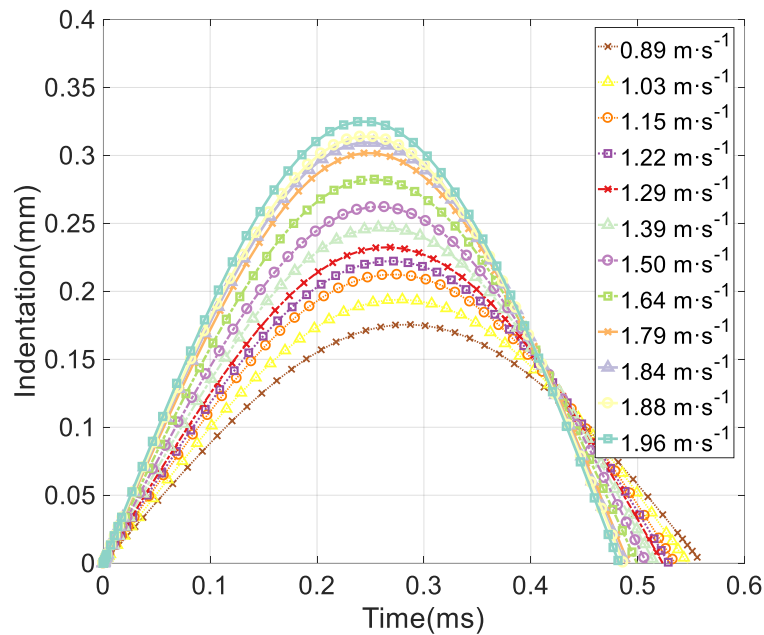
(f) $v = 1.96$ m·s^{-1}

1   **Fig. 8** Validation with the experimental data of PVB LG ID1-10
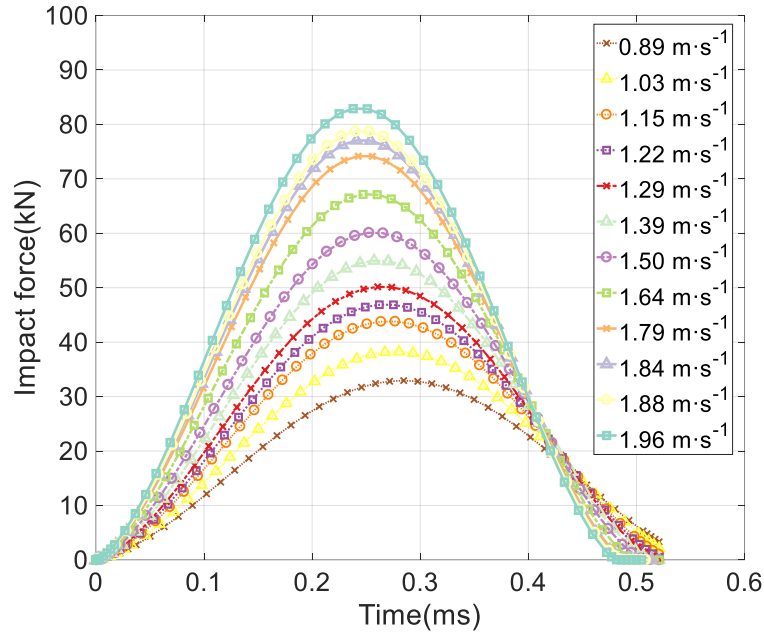
(a) Impact force with increasing impact velocities

(b) Indentation with increasing impact velocities

1   **Fig. 9** Impact force and indentation with increasing impact velocities in PVB LG ID1-10

2   The analytical impact force and indentation motion with increasing impact velocities in PVB

3   LG ID1-10 are shown in **Fig. 9** (a, b), respectively. It can be seen that the duration of indentation is

4   within (0.48 ms, 0.56 ms), showing a rapid hit of impactor head into glass material. The indentation

5   increases from 0.175 mm at velocity of 0.89 m·s^{-1} to 0.326 mm at velocity of 1.96 m·s^{-1}, where the

6   downward velocity of LG panel approaches that of impactor head. The relative movement decreases

1   and hence indentation does not further increase. Meanwhile, the peak impact force increases from

2   32.2 kN at velocity of 0.89 m·s⁻¹ to 82.9 kN at velocity of 1.96 m·s⁻¹.

3   The peak impact force from experimental and analytical results of tested PVB LG specimens

4   are collected and shown in **Fig. 10**. It is found that, the experimental and analytical peak force have

5   great consistency at lower impact velocity. With the impact velocity increases, the greater slope of

6   analytical result gradually leads to an overestimation of peak force when the impact velocity is

7   greater than 1.22 m·s⁻¹. The average difference between the experimental results and the theoretical

8   results is 2.76% and the standard deviation is 2.67.

9
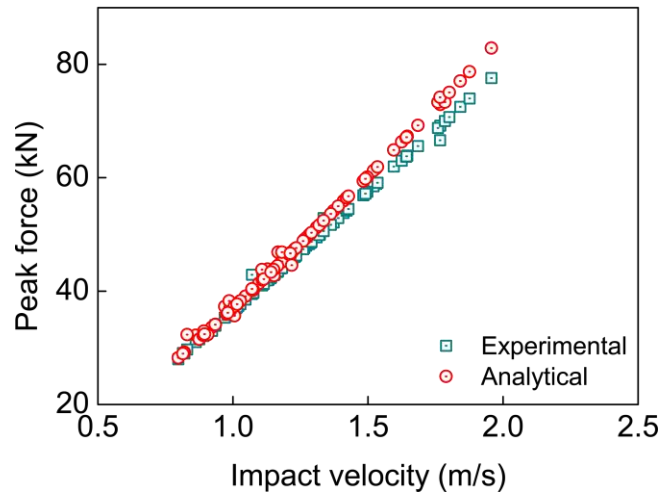
10   **Fig. 10** Collection of peak impact force from experimental and analytical results of PVB LG;

11   Difference =$[F_c(\text{analytical})-F_c(\text{experimental})]/ F_c(\text{experimental})\times 100\%$

12

13   **(2) SG laminated glass panels:**

14   The material properties of SG used in the validation of pre-crack behavior in SG LG panels are

15   as follows: elastic modulus: E_{SG} = 675 MPa; density: ρ_{SG} = 1100 kg·m⁻³; Poisson's ratio: μ_{SG} = 0.45.

16   Differing from PVB material, the elastic modulus of SG material is found to be relatively insensitive

17   to strain rate and presents an elastic modulus of nearly 500 MPa with strain rate lower than 100 s⁻¹

18   [59]. Considering that higher strain rate in this work will still enhance the elastic modulus of polymer,

19   a higher modulus of 675 MPa is determined for SG material based on the associated reports of SG

20   material. As the recorded impact velocity of specimen ID2-01 can cover the testing velocity range

21   in SG LG panels, it is adopted to validate the corresponding analytical results. Firstly, before

comparing the testing and analytical results in SG LGs, through overviewing the experimental result and giving a comparison between that from PVB LG and SG LG, for example, PVB LG in **Fig. 8** (a) and SG LG in **Fig. 12** (a) having similar impact velocity, it is found the impact force variation shares a close form and has similar characteristics of duration, oscillation and force peaks. It indicates that the elastic modulus of interlayer might not have significant influence on the pre-crack impact force response, as the force is mostly dependent on the elastic modulus of the contact material, i.e. glass material in the pre-crack stage. A sensitivity study is also performed to examine such conclusion. As shown in **Fig. 11**, elastic modulus ranging from 50 MPa to 1000 MPa are selected for the interlayer of 1.52 mm to investigate its effect on the pre-crack impact force. The impact velocity is determined to be 0.86 m·s^{-1}. The results show that the difference in the force curves with different elastic modulus of interlayer can be omitted. Therefore, in the pre-crack stage, it is rational to conclude that the interlayer types do not have great influence on the pre-crack behaviour, in particular, impact force.

However, it is also noting that in the subsequent test with impact failure which is not shown in this study, the tested SG LG panels are more likely to crack at a much lower impact velocity. This shows that the interlayer types can present their effect on triggering the fracture via other aspects. For example, SG material has greater adhesion property with the glass material when comparing with PVB material. Once the impact induced stress wave reaches the SG-glass interface, it will generate higher local strain at the interface. Thus, glass panel might be easier to fracture. On the other hand, in those cases with failure originating from the opposite side to the impact, the tensile stress wave is the predominant factor of triggering fracture. The difference in the viscoelasticity of interlayers will have various cushion effects on reducing or interrupting the stress wave propagation and hence present varying impact resistance of LG.
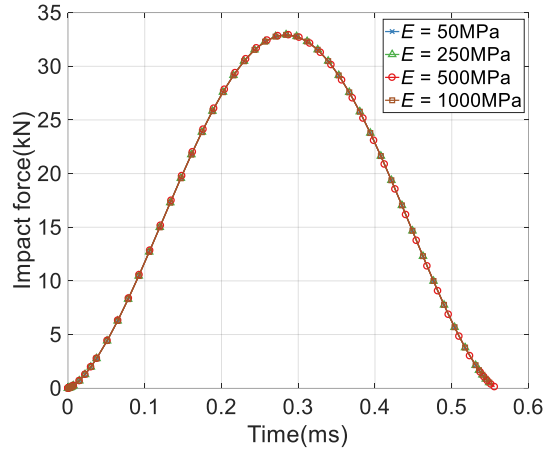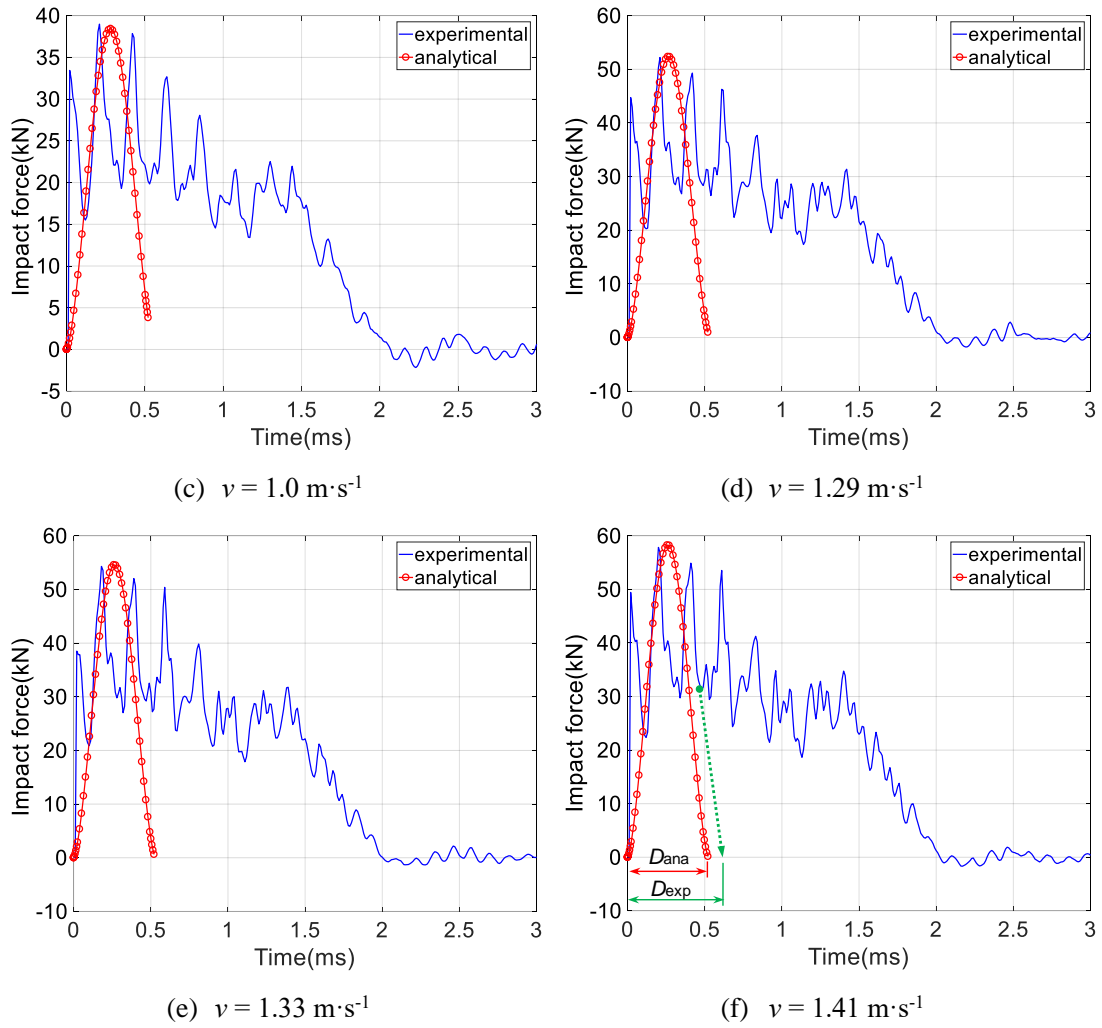
Fig. 11 Sensitivity of impact force to the elastic modulus of interlayer

Six cases from velocity of 0.86 m·s⁻¹ to 1.41 m·s⁻¹ are shown in **Fig. 12** to give a comparison between analytical result and experimental data. From **Fig. 12** (a), similar to the finding in PVB LG, it can also be seen that the analytical result increases with a close path to the rising stage of PeakA. The analytical peak force is 32.0 kN, which is slightly less than that of experimental result in PeakA (32.8 kN), showing a negligible difference. The analytical curve drops at nearly 0.29 ms and its decrease also follows a similar path to the declining stage of PeakB. It indicates that the results from proposed model can also map well with the testing data. From **Fig. 12** (b) to (f), it shows that in most cases the predicted duration (see D_{ana} in **Fig. 12** (f)) is underestimated when comparing with the expected experimental one (see D_{exp} in **Fig. 12** (f)). As the impact velocity increases, the absolute difference of peak force firstly decreases from the case of $v = 0.89$ m·s⁻¹ (0.8 kN) to that of $v = 1.29$ m·s⁻¹ (0.12 kN) and has another rise to that of $v = 1.41$ m·s⁻¹ (0.46 kN). Such difference is relatively small and hence the analytical result can be accepted.

(a) $v = 0.86$ m·s⁻¹ (b) $v = 0.89$ m·s⁻¹

26

(c) $v = 1.0 \text{ m·s}^{-1}$ (d) $v = 1.29 \text{ m·s}^{-1}$
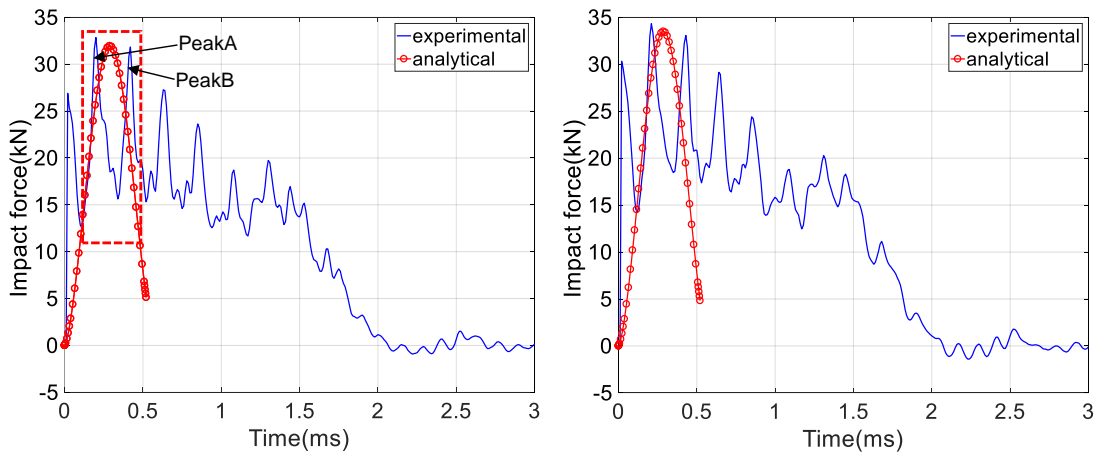
(e) $v = 1.33 \text{ m·s}^{-1}$ (f) $v = 1.41 \text{ m·s}^{-1}$

**Fig. 12** Validation with the experimental data of SG LG ID2-01

As above mentioned, the sensitivity study of impact force to the elastic modulus of interlayer shows that within a limited range of elastic modulus, the interlayer type will not present evident effect on the response, therefore the predicted impact force and indentation of SG LG follows the similar trend to that of PVB LG. **Fig. 13 错误!未找到引用源。** shows the analytical impact force and indentation motion with increasing impact velocities in SG LG ID2-01. In **Fig. 13** (b), the duration of indentation is within (0.52 ms, 0.58 ms) whilst the indentation increases from 0.168 mm at velocity of 0.86 m·s⁻¹ to 0.251 mm at velocity of 1.41 m·s⁻¹. Meanwhile, the peak impact force increases from 32.0 kN at velocity of 0.86 m·s⁻¹ to 58.3 kN at velocity of 1.41 m·s⁻¹.

Fig. 14 gives the collection of the peak impact force from experimental and analytical results of SG LG specimens. Overall, the experimental and analytical peak force still have good consistency in the examined velocity range. The difference between the experimental and analytical peak force

27

1   varies from -4.68% to 0.8%. The average difference and standard deviation are -1.96% and 1.48,

2   respectively. In the velocity range lower than 1.0 m·s^{-1}, the analytical prediction is slightly lower

3   than the testing data. Once the velocity exceeds 1.0 m·s^{-1}, the analytical result shows a trend of

4   being greater than the experimental one.
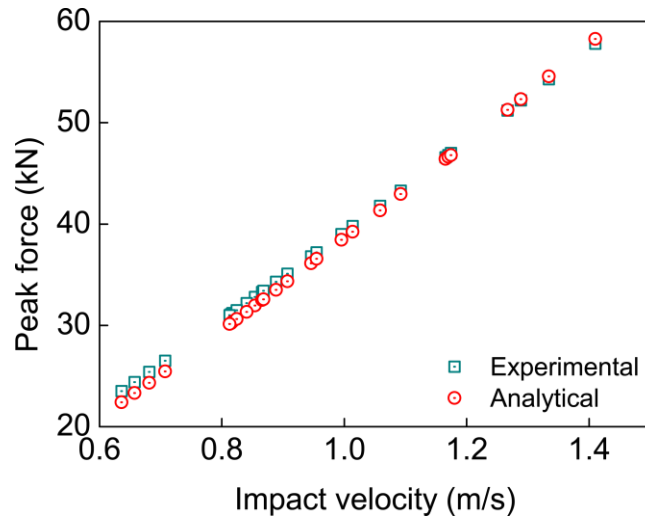
5
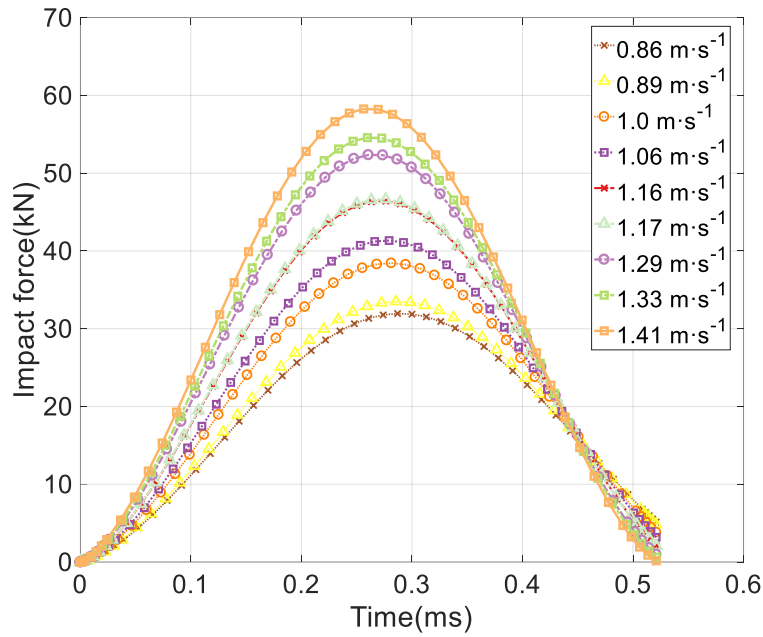
(a) Impact force with increasing impact velocities
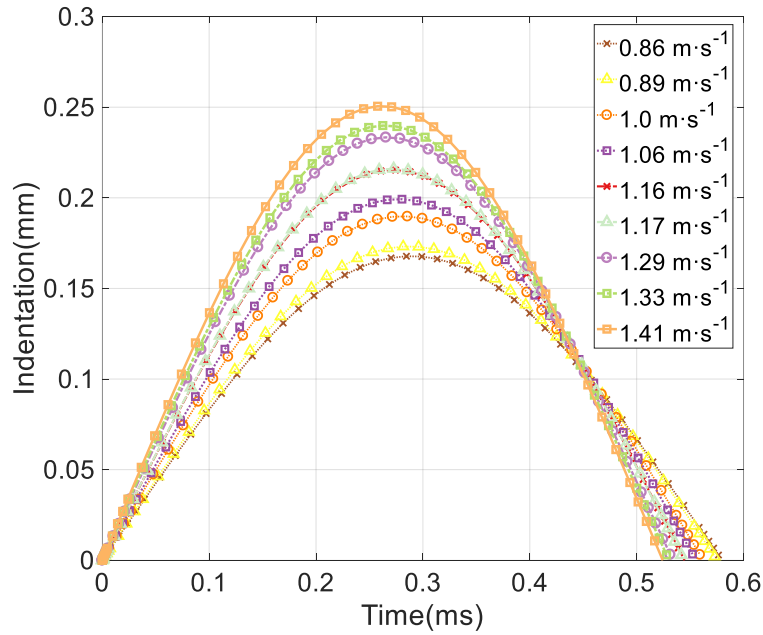
(b) Indentation with increasing impact velocities

6   **Fig. 13** Impact force and indentation with increasing impact velocities in SG LG ID2-01

1

2   **Fig. 14** Collection of peak impact force from experimental and analytical results of SG LG

3

4 5. Case study

5   Based on the findings from above study, a case study was designed and carried out to examine

6 the difference in the pre-crack impact response of the examined cases. A double layered LG panel

7 with 1.52 mm SG interlayer was set as a reference panel. Two cases using 1) a reference panel

8 laminated with extra safety window film (SWF), 2) a monolithic glass panel which can obtain

9 identical indentation to the reference panel in the impact with same velocity, were considered.

10   (1) Case 1:

11   The thickness of SWF was set as 4 mil, 8 mil and 14 mil, respectively. The thickness of SWF

12 is commonly expressed in 'mil', 1 mil equals to 0.0254 mm. This case was designed as it was found

13 the material at the contact side of LG panel significantly affected the indentation and impact force.

14 The impact velocity was set as 1.0 m·s^{-1}. SWF was simplified into the laminated polyethylene

15 terephthalate (PET) layers. The adhesives between PET layers as well as the coating were not

16 included. Material properties of PET are as follows: elastic modulus: E_{PET}= 3.8 GPa; density: ρ_{PET}

17 = 1350 kg·m^{-3}; Poisson's ratio: μ_{PET} = 0.38. In this case, the reference LG panel was fitted with the

18 SWF or without film.

(a) Impact force

(b) Indentation
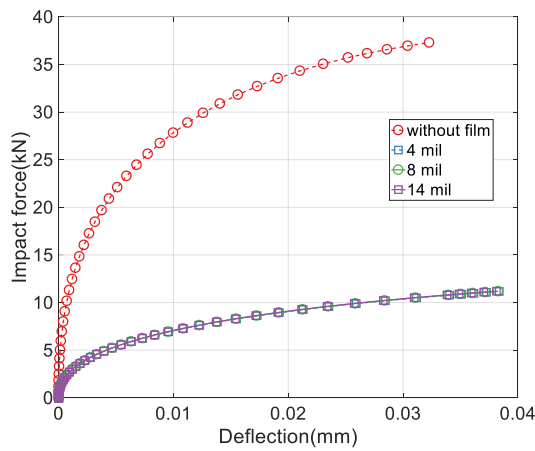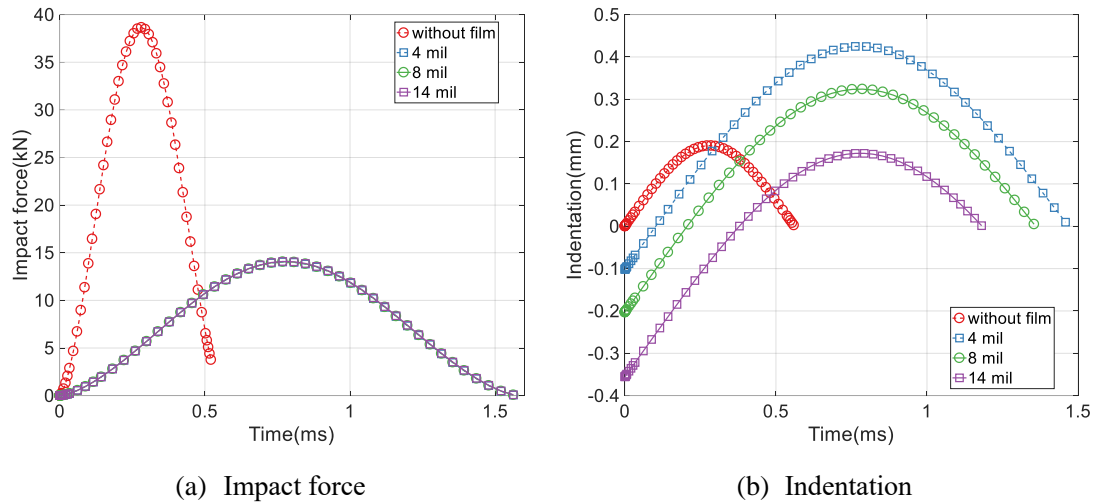
(c) Impact force – panel deflection

Fig. 15 The effect of the SWF on the pre-crack impact response of LG

The analytical results of the pre-crack impact response of the LG panels with or without SWF are given in **Fig. 15**. It is seen that the SWF can significantly reduce the impact force by more than 63% whereas the further increase of SWF thickness does not present significant influence on reducing the impact force. The curves of impact force (**Fig. 15** (a)) and force-deflection (**Fig. 15** (c)) from the LG panels with SWF are highly consistent. In these cases, the duration of the impact force also increases to nearly 1.56 ms. In **Fig. 15** (b), the obtained indentation from panels with SWF is not originated from zero, this is because the thickness of SWF has been deducted. It is seen that the application of a thin SWF (4 mil, 8 mil) does not generate the reduction of indentation, on the contrary, the indentation increa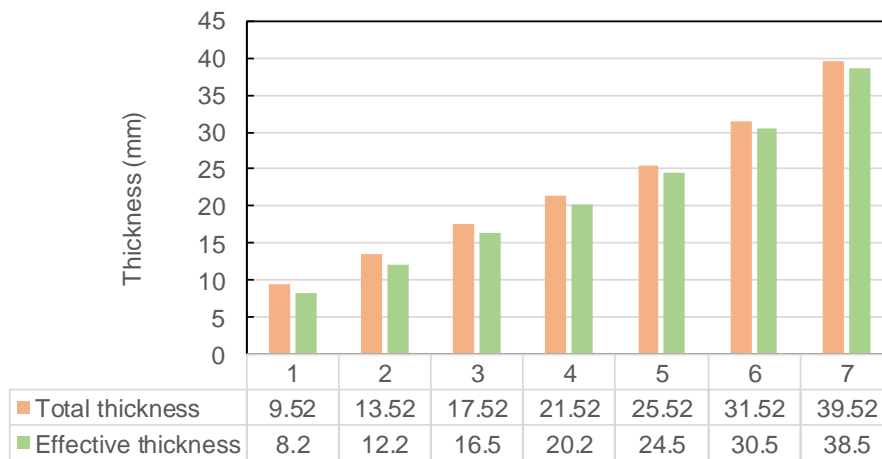ses more than 124% with a 4 mil SWF and 70% with 8 mil SWF. When the thickness of SWF increases to 14 mil, the indentation decreases to around 0.172 mm, which is lower than that (0.19 mm) from the panel without SWF. It can be concluded that the use of

30

1   SWF can significantly reduce the impact force by more than 63% with the examined impact velocity,

2   however the indentation can only see a decline when a 14 mil thick SWF is used.

3   (2) Case 2:

4   In this case, an effective thickness method was used to simplify the reference LG panel as a

5   monolithic glass panel. Differing from the traditional effective thickness [61] used in the design

6   code of structural glass [62] which approximates the same deflection or same stress in each glass

7   layer under static load, the monolithic glass panel in this case will have same indentation under

8   impact with same velocity. The effective thickness of LG panel using 1.52 mm SG interlayer and

9   glass layers with varying thickness from 4 mm to 19 mm was calculated by the proposed analytical

10   model. The results are shown in **Fig. 16**. The effective thickness is found to be slightly greater than

11   the thickness of two glass layers.

|	1	2	3	4	5	6	7
Total thickness	9.52	13.52	17.52	21.52	25.52	31.52	39.52
Effective thickness	8.2	12.2	16.5	20.2	24.5	30.5	38.5

12   **Fig. 16** Collection and comparison of effective thickness and total thickness

13   **Fig. 17** shows the validation of the pre-crack impact response using effective thickness

14   (monolithic glass) and total thickness (laminated glass) under impact velocity of 1.0 m·s^{-1}. The time

15   history of impact force, indentation, the relationship of impact force and glass panel deflection are

16   shown in **Fig. 17** (a) to (c), respectively. It is seen that with lower glass thickness the impact response

17   of laminated glass tends to be slightly smaller than that of monolithic glass. Overall, the pre-crack

18   impact response using effective thickness is consistent with that using total thickness, indicating the

19   reliable equivalence.

31
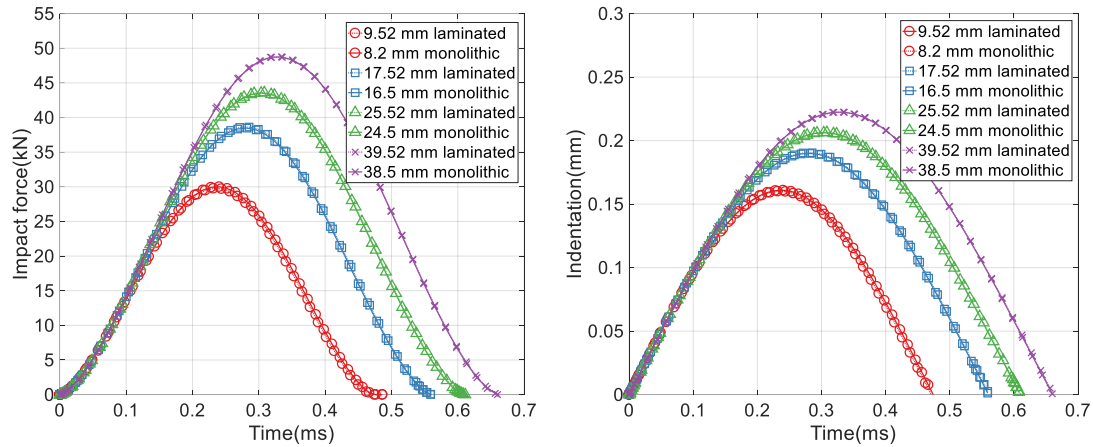
(a) Impact force

(b) Indentation
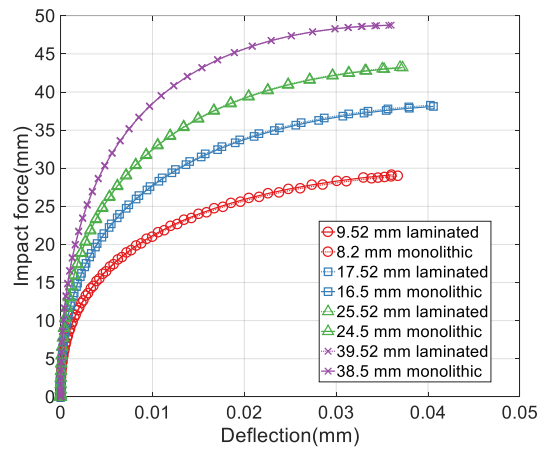
(c) Impact force – panel deflection

Fig. 17 Validation of the impact response using effective thickness and total thickness

A sensitivity study of the impact velocity on the impact response was also conducted. The impact velocity varies from 0.6 m·s^{-1} to 2.0 m·s^{-1}. The time history of impact force, indentation, the relationship of impact force and glass panel deflection are shown in **Fig. 18** (a) to (c), respectively. It can be seen that the impact response of monolithic glass using effective thickness can achieve good consistency with that of laminated glass panel, showing that the effective thickness based on the equivalence of indentation is reliable in the low velocity impact.

(a) Impact force (b) Indentation

(c) Impact force – panel deflection
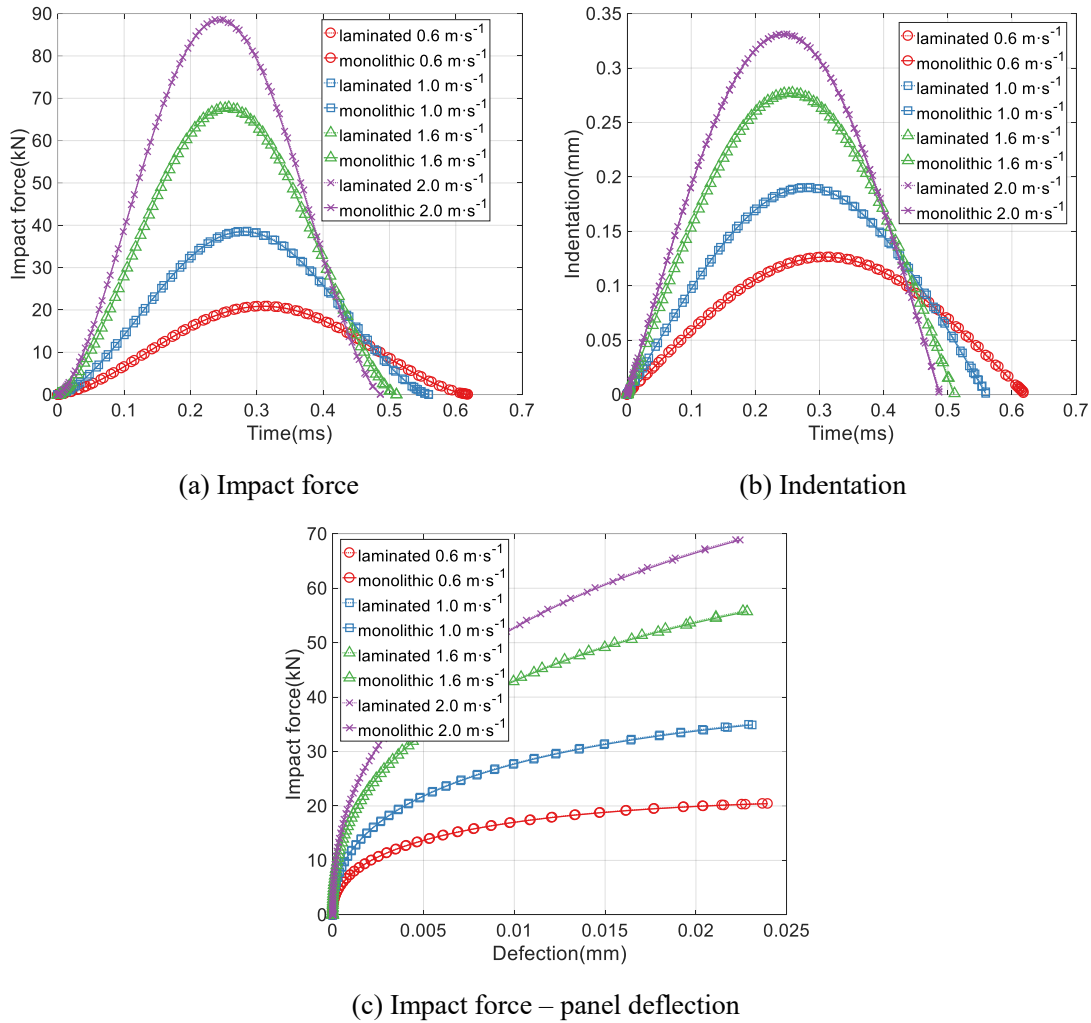
1   **Fig. 18** Validation of the impact response using effective thickness under various impact velocities

2

3   6. Concluding remarks

4   In this study, a nonlinear analytical model was developed for predicting the pre-crack impact

5   force response and its indentation behaviour of structural laminated glass under hard body impact

6   with low velocity. The analytical results were validated with those obtained from a series of impact

7   tests on square PVB and SG laminated glass panels. The results show that the proposed model can

8   well capture the examined feature and satisfactory impact force response, although with the velocity

9   increase the analytical model will tend to slightly overestimate the peak impact force. It is also found

10   that the pre-crack impact force response of SG laminated glass panels exhibits high consistency

11   with that using PVB interlayers, because the elastic property of the material at the contact layer,

12   glass, dominants such behaviour.

13   It was followed by two case studies which focused on the influence of the safety window film

on reducing impact response, and the applicability of a proposed effective thickness method of LG based on the indentation equivalence. The results show that using the film can reduce more than 63% of the impact force, however the variation of film thickness does not show further promotion. A 14 mil thick film can also reduce the impact indentation whereas less thick film might increase the indentation. The validation of the proposed effective thickness method shows its reliability in the application of low velocity impact.

Data availability

The data that supports the findings of this study are available within the article.

CRediT authorship contribution statement

Xuhao Huang: Methodology, Writing – Original Draft, Data curation. **Xing-er Wang**: Writing – Original Draft, Investigation, Funding acquisition. **Jian Yang**: Writing – Review & Editing, Supervision, Funding acquisition. **Zhufeng Pan**: Validation, Data curation. **Feiliang Wang**: Writing – Review & Editing, Formal analysis. **Iftikhar Azim**: Writing – Review & Editing.

Declaration of Competing Interest

The authors declare that they have no known competing financial interests or personal relationships that could have appeared to influence the work reported in this paper.

Acknowledgement

Appendix A

In Eq. (10), the coefficients I_i can be calculated as:

$$(I_1, I_2, I_3, I_4, I_5, I_7) = \sum_{k=1}^{N} \int_{h_{k-1}}^{h_k} \rho_k (1, Z, Z^2, Z^3, Z^4, Z^6) dZ , \qquad (A.1)$$

and

$$\bar{I}_2 = I_2 - \frac{4I_4}{3h^2}, \quad \bar{I}_3 = I_3 - \frac{8I_5}{3h^2} + \frac{16I_7}{9h^4}, \quad \bar{I}_5 = I_5 - \frac{4I_7}{3h^2}$$

$$I_8 = \frac{I_2 \bar{I}_2}{I_1} - \frac{4\bar{I}_5}{3h^2} - \bar{I}_3, \quad I_9 = \frac{4\bar{I}_5}{3h^2} - \frac{4\bar{I}_2 I_4}{3h^2 I_1}, \quad I_{10} = \frac{\left(\bar{I}_2\right)^2}{I_1} - \bar{I}_3 . \qquad (A.2)$$

The matrices in the Eqs.(19)-(20) are derived in Shen [63].

$$\begin{bmatrix} A_{ij}^* & E_{ij}^* \\ B_{ij}^* & F_{ij}^* \\ D_{ij}^* & H_{ij}^* \end{bmatrix} = \begin{bmatrix} A_{ij}^{-1} & -A_{ij}^{-1} E_{ij} \\ -A_{ij}^{-1} B_{ij} & F_{ij} - E_{ij} A_{ij}^{-1} B_{ij} \\ D_{ij} - B_{ij} A_{ij}^{-1} B_{ij} & H_{ij} - E_{ij} A_{ij}^{-1} E_{ij} \end{bmatrix}, (i,j=1,2,6) \qquad (A.3)$$

in which A_{ij}, B_{ij}, D_{ij}, etc. are the LG panels stiffnesses, which are obtained as follow

$$\begin{bmatrix} A_{ij} & B_{ij} & D_{ij} \\ E_{ij} & F_{ij} & H_{ij} \end{bmatrix} = \sum_{k=1}^{N} \int_{h_{k-1}}^{h_k} (\bar{Q}_{ij})_k \begin{bmatrix} 1 & Z & Z^2 \\ Z^3 & Z^4 & Z^6 \end{bmatrix} dZ \quad (i,j=1,2,6) \qquad (A.4)$$

$$\begin{bmatrix} A_{ij} \\ D_{ij} \\ F_{ij} \end{bmatrix} = \sum_{k=1}^{N} \int_{h_{k-1}}^{h_k} (\bar{Q}_{ij})_k \begin{bmatrix} 1 \\ Z^2 \\ Z^4 \end{bmatrix} dZ \qquad (i,j=4,5) \qquad (A.5)$$

where $\bar{Q}_{ij}$ are the component of the transformed lamina stiffness matrix. For the isotropic

materials, $\bar{Q}_{ij}$ are evaluated as follows:

$$\begin{bmatrix} \bar{Q}_{11} & \bar{Q}_{12} & \bar{Q}_{16} \\ \bar{Q}_{22} & \bar{Q}_{26} & \bar{Q}_{66} \\ \bar{Q}_{44} & \bar{Q}_{45} & \bar{Q}_{55} \end{bmatrix}_k = \begin{bmatrix} Q_{11} & Q_{12} & 0 \\ Q_{22} & 0 & Q_{66} \\ Q_{44} & 0 & Q_{55} \end{bmatrix}_k \qquad (A.6)$$

$$\begin{bmatrix} Q_{11} \\ Q_{22} \\ Q_{12} \end{bmatrix}_k = \frac{1}{1 - \nu_{12}\nu_{21}} \begin{bmatrix} E_{11} \\ E_{22} \\ \nu_{21}E_{11} \end{bmatrix}_k, \begin{bmatrix} Q_{44} \\ Q_{55} \\ Q_{66} \end{bmatrix}_k = \begin{bmatrix} G_{23} \\ G_{13} \\ G_{12} \end{bmatrix}_k . \qquad (A.7)$$

References

[1] Saputra A, Behnke R, Xing W, Song C, Schneider J, Kaliske M. Numerical representation of fracture patterns and post-fracture load-bearing performance of thermally prestressed glass with polymer foil. Engineering Structures. 2021;226:111318.

[2] Wang X-E, Meng Y, Yang J, Huang X, Wang F, Xu H. Optimal kernel extreme learning machine model for predicting the fracture state and impact response of laminated glass panels. Thin-Walled Structures. 2021;162:107541.

[3] Wang X-e, Yang J, Pan Z, Wang F, Meng Y, Zhu Y. Exploratory investigation into the post-fracture model of laminated tempered glass using combined Voronoi-FDEM approach. International Journal of Mechanical Sciences. 2021;190:105989.

[4] Pelayo F, Lamela-Rey MJ, Muniz-Calvente M, López-Aenlle M, Álvarez-Vázquez A, Fernández-Canteli A. Study of the time-temperature-dependent behaviour of PVB: Application to laminated glass elements. Thin-Walled Structures. 2017;119:324-31.

[5] Centelles X, Pelayo F, Lamela-Rey MJ, Fernández AI, Salgado-Pizarro R, Castro JR, et al. Viscoelastic characterization of seven laminated glass interlayer materials from static tests. Construction and Building Materials. 2021;279:122503.

[6] Mohagheghian I, Wang Y, Jiang L, Zhang X, Guo X, Yan Y, et al. Quasi-static bending and low velocity impact performance of monolithic and laminated glass windows employing chemically strengthened glass. European Journal of Mechanics - A/Solids. 2017;63:165-86.

[7] Zhang X, Liu H, Maharaj C, Zheng M, Mohagheghian I, Zhang G, et al. Impact response of laminated glass with varying interlayer materials. International Journal of Impact Engineering. 2020;139:103505.

[8] Zhang X, Hao H, Ma G. Laboratory test and numerical simulation of laminated glass window vulnerability to debris impact. International Journal of Impact Engineering. 2013;55(5):49-62.

[9] Mohagheghian I, Charalambides MN, Wang Y, Jiang L, Zhang X, Yan Y, et al. Effect of the polymer interlayer on the high-velocity soft impact response of laminated glass plates. International Journal of Impact Engineering. 2018;120:150-70.

[10] Mohagheghian I, Wang Y, Zhou J, Yu L, Guo X, Yan Y, et al. Deformation and damage mechanisms of laminated glass windows subjected to high velocity soft impact. International Journal of Solids and Structures. 2017;109:46-62.

[11] Zhang X, Mohammed IK, Zheng M, Wu N, Mohagheghian I, Zhang G, et al. Temperature effects on the low velocity impact response of laminated glass with different types of interlayer materials. International Journal of Impact Engineering. 2019;124:9-22.

[12] Wang X-e, Yang J, Chong WTA, Qiao P, Peng S, Huang X. Post-fracture performance of laminated glass panels under consecutive hard body impacts. Composite Structures. 2020;254:112777.

[13] Chen Y, He K, Han S, Yuan Y. Experimental study on three-layer tempered glass panel on quadrilateral simple bearing under local uniformly distributed load. Thin-Walled Structures. 2019;139:294-309.

[14] Guo Z, Li Z, Chen Y. Experimental study on mechanical behavior of double-layer toughened sandwich glass with two-side simple support. Thin-Walled Structures. 2021;158:107154.

[15] Schneider J, Schula S. Simulating soft body impact on glass structures. Proceedings of the Institution of Civil Engineers - Structures and Buildings. 2016;169(6):416-31.

[16] Gao W, Liu X, Chen S, Bui TQ, Yoshimura S. A cohesive zone based DE/FE coupling approach for

36

interfacial debonding analysis of laminated glass. Theoretical and Applied Fracture Mechanics. 2020;108:102668.

[17] Knight CG, Swain MV, Chaudhri MM. Impact of small steel spheres on glass surfaces. Journal of Materials Science. 1977;12(8):1573-86.

[18] Saxe TJ, Behr RA, Minor JE, Kremer PA, Dharani LR. Effects of Missile Size and Glass Type on Impact Resistance of "Sacrificial Ply" Laminated Glass. Journal of Architectural Engineering. 2002;8(1):24-39.

[19] Pyttel T, Liebertz H, Cai J. Failure criterion for laminated glass under impact loading and its application in finite element simulation. International Journal of Impact Engineering. 2011;38(4):252-63.

[20] Wang X-e, Yang J, Liu Q, Zhao C. Experimental investigations into SGP laminated glass under low velocity impact. International Journal of Impact Engineering. 2018;122:91-108.

[21] Liu B, Xu T, Xu X, Wang Y, Sun Y, Li Y. Energy absorption mechanism of polyvinyl butyral laminated windshield subjected to head impact: Experiment and numerical simulations. International Journal of Impact Engineering. 2016;90:26-36.

[22] Yuan Y, Xu C, Xu T, Sun Y, Liu B, Li Y. An analytical model for deformation and damage of rectangular laminated glass under low-velocity impact. Composite Structures. 2017;176:833-43.

[23] Shahriari M, Saeidi Googarchin H. Prediction of vehicle impact speed based on the post-cracking behavior of automotive PVB laminated glass: Analytical modeling and numerical cohesive zone modeling. Engineering Fracture Mechanics. 2020;240:107352.

[24] Osnes K, Hopperstad OS, Børvik T. Rate dependent fracture of monolithic and laminated glass: Experiments and simulations. Engineering Structures. 2020;212:110516.

[25] Ha YD. An extended ghost interlayer model in peridynamic theory for high-velocity impact fracture of laminated glass structures. Computers & Mathematics with Applications. 2020;80(5):744-61.

[26] Chen S, Chen H, Mitsume N, Morita N, Bui TQ, Gao W, et al. A nodal-based Lagrange multiplier/cohesive zone approach for dynamic interfacial cracking analysis of thin-walled laminated composite structures. Composite Structures. 2021;256:113112.

[27] Wang X-e, Yang J, Wang F, Liu Q-f, Xu H. Simulating the impact damage of laminated glass considering mixed mode delamination using FEM/DEM. Composite Structures. 2018;202:1239-52.

[28] Choi IH, Kim IG, Ahn SM, Yeom CH. Analytical and experimental studies on the low-velocity impact response and damage of composite laminates under in-plane loads with structural damping effects. Composites Science and Technology. 2010;70(10):1513-22.

[29] Singh H, Mahajan P. Analytical modeling of low velocity large mass impact on composite plate including damage evolution. Composite Structures. 2016;149:79-92.

[30] Wang H, Yin X, Hao H, Chen W, Yu B. The correlation of theoretical contact models for normal elastic-plastic impacts. International Journal of Solids and Structures. 2020;182-183:15-33.

[31] Huang X-H, Yang J, Wang X-E, Azim I. Combined analytical and numerical approach for auxetic FG-CNTRC plate subjected to a sudden load. Engineering with Computers. 2020.

[32] Baba MN, Dogaru F, Guiman MV. Low Velocity Impact Response of Laminate Rectangular Plates Made of Carbon Fiber Reinforced Plastics. Procedia Manufacturing. 2020;46:95-102.

[33] Rühl A, Kolling S, Schneider J. A transparent three-layered laminate composed of poly(methyl methacrylate) and thermoplastic polyurethane subjected to low-velocity impact. International Journal of Impact Engineering. 2020;136:103419.

[34] Amabili M, Balasubramanian P, Garziera R, Royer-Carfagni G. Blast loads and nonlinear vibrations

of laminated glass plates in an enhanced shear deformation theory. Composite Structures. 2020;252:112720.

[35] Amabili M. Nonlinear damping in nonlinear vibrations of rectangular plates: Derivation from viscoelasticity and experimental validation. Journal of the Mechanics and Physics of Solids. 2018;118:275-92.

[36] Galuppi L, Royer-Carfagni G. Analytical approach a la Newmark for curved laminated glass. Composites Part B-Engineering. 2015;76:65-78.

[37] Del Linz P, Liang X, Hooper PA, Wang LZ, Dear JP. An analytical solution for pre-crack behaviour of laminated glass under blast loading. Composite Structures. 2016;144:156-64.

[38] Standardization Administration of China. GB 15763.2 Safety glazing materials in building - Part 2: Tempered glass. Beijing: Standards Press of China; 2005.

[39] Standardization Administration of China. GB 15763.3 Safety glazing materials in building - Part 3: Laminated glass. Beijing: Standards Press of China; 2009.

[40] Standardization Administration of China. GB/T 528 Rubber, vulcanized or thermoplastic - Determination of tensile stress-strain properties. Beijing: Standards Press of China; 2009.

[41] Chaudhri MM, Liangyi C. The orientation of the Hertzian cone crack in soda-lime glass formed by oblique dynamic and quasi-static loading with a hard sphere. Journal of Materials Science. 1989;24(10):3441-8.

[42] Janda T, Schmidt J, Hála P, Konrád P, Zemanová A, Sovják R, et al. Reduced order models of elastic glass plate under low velocity impact. Computers & Structures. 2021;244:106430.

[43] Abrate S. Localized Impact on Sandwich Structures With Laminated Facings. Applied Mechanics Reviews. 1997;50(2):69-82.

[44] Greszczuk LB. Damage in composite materials due to low velocity impact. Impact dynamics. 1982:55-94.

[45] Shivakumar KN, Elber W, Illg W. Prediction of impact force and duration due to low-velocity impact on circular composite laminates. Journal of Applied Mechanics. 1985;52(3):674-80.

[46] Olsson R. Closed form prediction of peak load and delamination onset under small mass impact. Composite Structures. 2003;59(3):341-9.

[47] Reddy JN. A simple higher-order theory for laminated composite plates. Journal of Applied Mechanics. 1984;51(4):745-52.

[48] Amabili M. Nonlinear damping in large-amplitude vibrations: modelling and experiments. Nonlinear Dynamics. 2018;93(1):5-18.

[49] Amabili M. Derivation of nonlinear damping from viscoelasticity in case of nonlinear vibrations. Nonlinear Dynamics. 2019;97(3):1785-97.

[50] Shen H-S. A two-step perturbation method in nonlinear analysis of beams, plates and shells: John Wiley & Sons; 2013.

[51] Zhang D. High-order analytical solutions and convergence discussions of the 2-step perturbation method for Euler-Bernoulli beams. Applied Mathematics and Mechanics. 2019;40:620-9.

[52] Shen HS, Xiang Y, Fan Y. Large amplitude vibration of doubly curved FG-GRC laminated panels in thermal environments. Nanotechnology Reviews. 2019;8(1):467-83.

[53] She G-L, Yuan F-G, Ren Y-R, Liu H-B, Xiao W-S. Nonlinear bending and vibration analysis of functionally graded porous tubes via a nonlocal strain gradient theory. Composite Structures. 2018;203:614-23.

[54] Yang J, Huang X-H, Shen H-S. Nonlinear vibration of temperature-dependent FG-CNTRC

laminated plates with negative Poisson's ratio. Thin-Walled Structures. 2020;148:106514.

[55] Babaei H, Kiani Y, Eslami MR. Large amplitude free vibration analysis of shear deformable FGM shallow arches on nonlinear elastic foundation. Thin-Walled Structures. 2019;144:106237.

[56] Fan Y, Wang Y. The effect of negative Poisson's ratio on the low-velocity impact response of an auxetic nanocomposite laminate beam. International Journal of Mechanics and Materials in Design. 2021;17(1):153-69.

[57] Song M, Li X, Kitipornchai S, Bi Q, Yang J. Low-velocity impact response of geometrically nonlinear functionally graded graphene platelet-reinforced nanocomposite plates. Nonlinear Dynamics. 2019;95(3):2333-52.

[58] Jam JE, Kiani Y. Low velocity impact response of functionally graded carbon nanotube reinforced composite beams in thermal environment. Composite Structures. 2015;132:35-43.

[59] Bennison S, Sloan J, Kistunas D, Buehler P, Amos T, Smith C. Laminated glass for blast mitigation: role of interlayer properties.   Proceedings of glass processing days; Tampere, Finland2005.

[60] Zhang X, Hao H, Shi Y, Cui J. The mechanical properties of Polyvinyl Butyral (PVB) at high strain rates. Construction and Building Materials. 2015;93:404-15.

[61] Galuppi L, Royer-Carfagni G. Enhanced effective thickness of multi-layered laminated glass. Composites Part B: Engineering. 2014;64:202-13.

[62] CNR – Advisory Committee on Technical Recommendations for Construction. CNR DT 210 Guide for the Design, Construction and Control of Buildings with Structural Glass Elements. Roma2013.

[63] Shen H-S. Kármán-type equations for a higher-order shear deformation plate theory and its use in the thermal postbuckling analysis. Applied Mathematics and Mechanics. 1997;18(12):1137-52.